Dissertation
submitted to the
Combined Faculty of
Natural Sciences and Mathematics
of the
Ruperto-Carola-University of Heidelberg,
Germany
for the degree of
Doctor of Natural Sciences

Put forward by

Gustavo Dopcke
born in: Três de Maio, Brazil

Oral examination: February 6, 2013

On the physics of the low metallicity IMF

Referees:

Prof. Dr. Eva K. Grebel

Prof. Dr. Ralf S. Klessen

Einfluss niedriger Metallizität auf die anfängliche stellare Massenfunktion – Eine fundamentale Frage im Zusammenhang mit Strukturentstehung beschäftigt sich mit dem Übergang von massereichen primordialen Sternen zu Sternen der Population I/II mit typischen Massen von weniger als 1 $M_\odot$ und insbesondere mit dem physikalischen Mechanismus, welcher diesen Übergang einleitet.

Thema dieser Arbeit ist es die physikalischen Mechanismen zu untersuchen, die einen solchen Übergang zur Folge haben und die stellare IMF in den frühen Stadien des Universums formen. Mit diesem Ziel führen wir eine Reihe hydrodynamischer Simulationen durch, welche sogenannte Sink-Teilchen enthalten, die kontrahierende Protosterne repräsentieren.

Insgesamt werden acht Simulationen durchgeführt. In allen Fällen finden wir Hinweise auf Fragmentierung, weshalb wir schlussfolgern, dass es keine kritische Metallizität gibt, unterhalb welcher Fragmentierung unmöglich ist. Dennoch gibt es eine deutliche Veränderung der charakteristischen Masse der Wolken bei $Z = 10^{-4} Z_\odot$.

Ausgehend von der Entwicklung der simulierten Cluster entwickeln wir ein Modell für die stellare IMF. Damit können wir Ergebnisse von Simulationen sowie Beobachtungen des Orion Nebel Clusters erklären. Abschließend finden wir, dass die resultierende stellare Massenverteilung stark von der charakteristischen Masse des Clusters und von der Art der Massenakkretion abhängt.

On the physics of the low metallicity IMF – A fundamental question in the context of structure formation concerns the transition from massive primordial stars to Population I/II stars with typical masses of less than 1 $M_\odot$, and in particular the physical mechanisms inducing this transition.

The purpose of this work is to study the physical mechanisms that shape the stellar IMF at the early stages of the Universe. With this aim, we perform a set of eight hydrodynamic simulations that include sink particles representing contracting protostars. Evidence for fragmentation was found in all cases, and hence we conclude that there is no critical metallicity below which fragmentation is impossible. Nevertheless, there is a clear change in the characteristic mass of the clouds at $Z = 10^{-4} Z_\odot$.

Moreover, we develop a model for the stellar IMF, which accounts for the evolution of simulated clusters. With that, we can recover results from hydrodynamic simulations, and also observations of the Orion Nebulae Cluster. Finally, we find that the resultant stellar mass distribution is highly dependent on the characteristic mass of the cluster, and the mode of mass accretion.

A Pilar, que está sempre comigo.

Contents

Chapter 1

Introduction

The synthesis of the first elements in the Universe started just after the Big Bang, with the formation of hydrogen, helium and small traces of lithium and beryllium. This material fell onto dark matter haloes to form the first stars, the so called Population III (Pop. III). Such stellar population categories are divided in three, with the youngest and most metal rich being Pop. I, and the oldest and metal-free stars being called Pop. III. Moreover, metallicity in astrophysics is represented by the letter Z, and refers to the fraction of elements heavier than helium, which is not the same definition for metals as in chemistry. Also, in the end of their lives, the stars explode as supernovae, event which releases metals in the interstellar medium. The future generation inherit these metals, and over time, the Universe experience an increase in the fraction of heavy elements. Pop. II, for instance, come from the clouds that were enriched by the Pop. III supernovae, and are the oldest generation of stars observed in our galaxy. After the death of those, they also expel metals in the media and the new stars which form are the youngest and most metal rich, the Pop. I.

The first burst of star formation in the Universe is thought to give rise to massive stars, with current theory predicting characteristic masses considerably above the solar value (Abel et al. 2002; Bromm et al. 2002; Yoshida et al. 2008; Clark et al. 2011b; Greif et al. 2011a). In addition to that, observational data require a stellar mass distribution dominated by massive stars to explain the characteristics of some Galactic globular clusters (Marks et al. 2012; Kroupa et al. 2011), and also the high fraction of extremely metal-poor stars that are C-rich (Suda et al. 2012). Massive stars evolve quickly, and thus have short life. In addition to that, when these stars die, they explode as supernovae and free heavy elements (Heger & Woosley 2002) to the interstellar medium (ISM), which enrich the material that future generations of

stars will form. Since most of Pop. III are massive, therefore have short-life, few Pop. III should have survived to be observed now. Moreover, the later accretion of metal-enriched gas may alter the surface of the Pop. III born stars, making them undistinguishable from Pop. II/I. Such effect however, is easily prevented if the stars are ejected from the center of the cloud where they originated (Johnson & Khochfar 2011). Likewise, the object forming in the center of the cloud could end its life in a black hole (Heger et al. 2003), before forming low-mass (thus long-lived) stars. If this happens, such object would form jets which pollute the media. Finally, even the oldest observed stars still have few heavy elements and thus the existence of a metal-free star remains a puzzle.

As for the site of their formation, one has to look at the first structures that could reach sufficient density to trigger star formation. The current theory for the present appearance of the Universe predicts that gravitational amplification of matter density fluctuations lead to the formation of clumpy structures. Moreover, the standard model based on cold dark matter (CDM) shows that structures form hierarchically, with smaller amplitudes of mass forming first. In this picture, the first objects were formed in low-mass haloes ($\sim 10^6 M_\odot$), in the deep of their potential well, and at redshift around 30. In such conditions, gas can cool via hydrogen cooling enhancing the gravitational collapse (Bromm & Larson 2004). These objects will be the population which terminate with the dark ages by emitting the first light (Reed et al. 2005).

Once the life of the fist stars end, their explosion will pollute the environment, with simulations showing that enrichment of 100 kpc to the level of 10^{-4} times the solar value could be achieved within ~ 300 Myr (Greif et al. 2010). Thus, the further generations of stars in this enriched gas form from redshift 30 to 10. The site for the formation of the low metallicity stars will be then newly enriched haloes, few million years after the explosion of the first supernovae.

The metals contained in these gas clouds can deplete into the form of dust (Schneider et al. 2012), which is an efficient coolant (Dopcke et al. 2011, 2012; Omukai et al. 2005) and can lead to the formation of low-mass (thus long-lived) stars. Nevertheless, the present-day star formation tends to yield stars with masses less than 1 $M_\odot$ (Kroupa 2002; Chabrier 2003), and so at some point in the evolution of the Universe there must have been a transition from primordial star formation to the mode of star formation we see today (Pop. II/I). This transition and the overall stellar population is important in particular for the process of reionization (Barkana & Loeb 2001; Schleicher et al. 2008).

Variations in the mode of star formation will have strong influence in

the mass distribution of stars. In the seminal work by Salpeter (Salpeter 1955), he raised the hipotesys of an initial mass function (IMF), which refers to the stellar mass distribution at the birth time. Such hypothesis enabled astrophysicists to make enormous advances in their research. The probability density function for high-mass stars could be fitted with a power-law distribution with a slope of -2.35. Miller & Scalo (1979) extended the work to low-mass objects and at this range, the IMF could be fitted with a half log-normal distribution.

After the IMF hypothesis was stablished observationally, a model that explained the physical mechanism behind it. One successful attempt made by Zinnecker (1984), where they showed it was possible to explain the log-normal shape in the low-mass range. The process was by a hierarchical fragmentation, based on successive stages. After each stage, the fragment would have a fraction of the total mass. Mathematically, each star has a mass correspondent to a successive multiplication of the cloud mass. By taking the logarithm of both stellar mass and product operator, the last becomes a summation. Finally, by applying the Central Limit Theorem (Cramér 1946), the distribution is a Gaussian in log-mass.

Moreover, Bonnell et al. (2001a) extended Zinnecker (1984) version of the model for the high-mass part of the IMF. They found that clusters could have a mass spectrum with the slope for high-mass objects $-2.5 < \gamma < -2.0$, when the potential is stellar-dominated and accretion is proportional to the square of the stellar mass. However before being consistent with mass segregated clusters, the competitive accretion picture needs to assume an initial segregation in order to develop a γ steeper than -2.

A fundamental question in the context of structure formation concerns the transition from massive primordial to Pop. I/II stars and in particular the physical mechanism inducing this transition. The discovery of extremely metal-poor stars like SDSS J102915+172927 suggests that it is cooling by dust, rather than via fine-structure metal lines, which enhances fragmentation even at metallicities of $\sim 10^{-4}\ Z_{\odot}$, thus changing the IMF already at early stages.

Dust then plays an important role in the puzzle of the never-observed metal-free Pop. III stars. Namely, it can determine the minimal metallicity ($Z_{\rm crit}$), at which the mode of star formation changes.

Therefore, new studies are required to address the question. The main questions concern exploring the low-metallicity ISM with particular emphasis on the implications of dust on star formation and the initial mass function (IMF). The results from such studies would thus shed light onto the earliest phases of galaxy and star formation. In light of upcoming large spectroscopic surveys, such as HERMES, Gaia-ESO, Pan-Starrs, it is timely and important

to explore low-metallicity star formation in much further detail.

1.1 Star formation at very low metallicities - thermal processes

When gas collapses to form stars, gravitational energy is transformed into thermal energy and unless this thermal energy can be dissipated in some fashion – such as via atomic fine-structure line emission, molecular rotational or vibrational line emission, or the heating of dust grains – it will eventually halt the collapse. In an adiabatic collapse, the further evolution can be approximated by a linear theory, and the number of fragments will be proportional to the number of Jeans masses in the cloud (Jeans 1902). In cases where these cooling processes are efficient, they can promote gravitational fragmentation (Bonnell et al. 2007), such that instead of forming one very massive clump or a number of clumps corresponding to the initial number of Jeans masses in the cloud, the cloud can instead form even more fragments. Therefore, if one aims to study the fragmentation of gas clouds, it is necessary to account for thermal processes.

If the gas is cooled only by molecular hydrogen emission, numerical simulations show that the stars should be very massive (Abel et al. 2002; Bromm et al. 2002; O'Shea & Norman 2007; Yoshida et al. 2008; Jappsen et al. 2009a). This happens because the H_2 cooling becomes inefficient for temperatures below 200 K and densities above 10^4 cm^{-3}. At this temperature and density, the Bonnor-Ebert mass is 1,000 times larger than in present-day molecular clouds, as can be seen from Eq. 1.1:

$$M_{BE} \approx 500 M_{\odot} \left(\frac{T}{200\mathrm{K}}\right)^{3/2} \left(\frac{n}{10^4 \mathrm{cm}^{-3}}\right)^{-1/2} \tag{1.1}$$

for an atomic gas with temperature T and number density n.

Also, the adequate primordial chemical network can have strong influence in the local Jeans mass. For instance, Glover & Abel (2008) showed that the minimum Jeans mass can increase by a factor of 2, when the chemical network includes cooling from H_2-H^+ collisions.

For metallicities higher than zero, other thermal effects start to play a role. The main coolants beyond H_2 in the case of non-zero metallicity that have been studied in the literature are CII and OI fine-structure and dust emission (Bromm et al. 2001; Bromm & Loeb 2003; Santoro & Shull 2006; Frebel et al. 2007; Jappsen et al. 2009a,b; Smith & Sigurdsson 2007; Smith et al. 2009a). By equating the CII or OI fine-structure cooling rate to the

compressional heating rate due to free-fall collapse, one can define critical abundances [C/H] = −3.5 and [O/H] = −3.0[1] for efficient metal-line cooling (Bromm & Loeb 2003).

If OI and CII are responsible for the change in the stellar initial mass function (IMF), then the Pop. II stars should have a combination of O and C abundances above the so-called "transition discriminant" $D_{\rm trans}$, where $D_{\rm trans} = \log(10^{[\rm C/H]} + 0.3 \cdot 10^{[\rm O/H]}) = -3.5$ (Frebel et al. 2007). The Jeans mass at densities where OI and CII can efficiently cool the gas is $\approx 10 M_{\odot}$, and none of the metal-poor stars observed to date can thus be explained by these cooling processes. Although most metal-poor stars lie above $D_{\rm trans}$, at least one star has been observed to lie below it (SDSS J102915+172927; Caffau et al. (2011)), and there are other objects that might also have abundances below $D_{\rm trans}$: CS30336-049 (Lai et al. 2008) and Scl07-50 (Tafelmeyer et al. 2010). Since SDSS J102915+172927 violates the transition discriminant, the scenario where OI and CII are responsible for the change in the IMF is not sustained, and there must be another mechanism that can cool the gas and lead to fragmentation and the formation of low mass stars. In fact, Schneider et al. (2012) proposed that dust has played a major role during the formation of this star by inducing fragmentation. Dust cooling models (e.g. Omukai et al. 2005, 2010; Dopcke et al. 2011; Schneider et al. 2006, 2012) predict a much lower critical metallicity ($Z_{\rm crit} \approx 10^{-4} - 10^{-6} Z_{\odot}$), with most of the uncertainty coming from the nature of the dust in high-redshift galaxies. Therefore, dust cooling is the most likely mechanism that can explain the existence of low mass stars with metallicities lower than $10^{-4} Z_{\odot}$, such as the SDSS J102915+172927 case.

A more complete study of the main heating and cooling mechanisms for various metallicities was done by Omukai et al. (2010). For the metal free case, the main coolants are H_2 and HD, and compressional PdV is the main heating process. H_2 counterbalance the PdV heating for number densities $n > 10^5$ cm^{-3}, and it efficiently cool the gas for $10^{10} < n/\rm cm^{-3} < 10^{13}$. For metallicities $Z > 10^{-5} Z_{\odot}$, the metal content begins to be important. Specially, H_2O becomes slightly efficient at $n \approx 10^{10}$ cm^{-3} and dust at $n > 10^{11}$ cm^{-3}. Under those circumstances, if one wants to study star formation at very low metallicities, a model that includes effects from H_2 and dust cooling is necessary.

At densities $n \gtrsim 10^{10}$ cm^{-3}, dust cooling becomes efficient (Dopcke et al. 2011, 2012; Omukai et al. 2010), because inelastic gas-grain collisions are

[1] $[\rm X/Y] = \log_{10}(\rm N_X/N_Y)_{\star} - \log_{10}(\rm N_X/N_Y)_{\odot}$, for elements X and Y, where $\star$ denotes the gas in question, and where $\rm N_X$ and $\rm N_Y$ are the mass fractions of the elements X and Y.

more frequent (Hollenbach & McKee 1979). Such cooling enhances fragmentation, and since it occurs at high densities, the distances between fragments can be very small (Dopcke et al. 2011, 2012; Omukai 2000; Omukai et al. 2005; Schneider et al. 2002, 2006; Schneider & Omukai 2010). In this regime, interactions between fragments will be common, and analytic models of fragmentation are thus unable to predict the mass distribution of the fragments. A full 3D numerical treatment, following the fragments, is needed.

Initial attempts at modeling fragmentation in low-metallicity gas were made by Tsuribe & Omukai (2006, 2008) and Clark et al. (2008). These studies described the thermal evolution of the gas using effective equations of state derived from the one-zone calculations of Omukai et al. (2005), and showed that the cooling provided by dust does indeed lead to fragmentation. This treatment assumes, however, that the gas temperature adjusts instantaneously to a new equilibrium whenever the density changes and hence ignores thermal inertia effects. This may thus overestimate the amount of fragmentation.

In Dopcke et al. (2011), we improved upon these previous treatments by solving the full thermal energy equation, and calculating the dust temperature through the energy equilibrium equation. We assumed that the only significant external heat source is the cosmic microwave background (CMB), and included its effects in the calculation of the dust temperature. We showed that model clouds with metallicities as low as $10^{-4} Z_\odot$ or $10^{-5} Z_\odot$ show indeed evidence for dust cooling and fragmentation, supporting the predictions by Tsuribe & Omukai (2006, 2008) and Clark et al. (2008). Even on larger scales, the presence of dust can significantly alter the chemistry by stimulating H_2 formation on dust grains (Cazaux & Spaans 2009; Latif et al. 2012). While dust thus generally enhances the cooling and decreases the Jeans mass, even moderate radiation backgrounds may efficiently rise the gas temperature at densities of up to $\sim 10^4$ cm^{-3} (e.g. Schleicher et al. 2010b). The interplay of these processes is thus particularly relevant for the initial conditions of star formation in the ISM.

1.2 Modeling the physical mechanisms that shape the IMF

The physical mechanism driving the shape of the IMF has been of intense debate during the last years. The supposed mechanisms include competitive accretion (Bonnell et al. 2011), supersonic turbulence (Chabrier & Hennebelle 2011), and radiation (Krumholz 2011). Exploring these processes

with numerically simulations requires codes that can incorporate the three mechanisms self-consistently.

Modeling competitive accretion requires an appropriate hydrodynamics code that can follow the accretion onto protostars. The Gadget-2 code (Springel 2005) has been widely used for this purpose, it is a smoothed particle hydrodynamics (SPH) implementation including a network for the chemistry at very low metallicities (Glover & Jappsen 2007). In this code, self-gravity is calculated via tree-structures, calculating contributions from nearby objects at high accuracy but combining more distant objects into groups, taking only their average contribution into account. In order to model the formation and accretion of protostars, the code includes a sink particle implementation (Bate et al. 1995a; Jappsen et al. 2005), replacing high-density SPH particles with sink particles. This procedure is necessary to continue the simulation with large enough time steps to follow the subsequent evolution, but also provides a natural way of following the accretion onto individual protostars.

In recent studies, it has been demonstrated that the method employed in Gadget-2 is capable of modeling supersonic turbulence, and reproduces the turbulent spectra that are typically found in grid codes (Price & Federrath 2010; Bauer & Springel 2011). Such supersonic turbulence is indeed the type of turbulence expected to prevail in the first galaxies (Wise & Abel 2007; Greif et al. 2008). To further improve on controlling the amount of artificial viscosity, the implementation for SPH codes of Cullen & Dehnen (2010) provides a suitable treatment both in the supersonic and the subsonic regime. Therefore, it enables to study turbulence and competitive accretion in various astrophysical problems.

1.3 Future surveys

Many large spectroscopic surveys are being planned for the following years, such as HERMES, Gaia-ESO, and Pan-Starrs. Although many of these are not specifically designed to look for EMP, their sheer size is expected to lead to the finding of at least some of them.

In addition to that, the fact that SDSS J1029151 +172927 was found out of a sample of only six candidates suggests that these stars may not be as rare as previously thought. Indeed, the inferred metallicity distribution in the SDSS catalogue shows a low-metallicity tail that seems to extend down to zero metallicity, hinting at the existence of a population of truly metal-free low mass stars in the Milky Way. Clearly, this needs to be confirmed by high-resolution follow-up spectroscopy. This is the goal of the ESO large program

ToPoS[2], to find and characterize hundreds of the most metal-poor stars in the SDSS catalogue. This unique database will provide valuable information about the oldest and most primitive stellar population in the Galaxy.

[2]ESO VLT: 120h x-shooter and 30h UVES time, PI: Elisabetta Caffau, proposal 189.D-0165

Chapter 2

What can low-resolution simulations teach us?

Low resolution simulations help to get a quick insight on the most important physical mechanisms that govern your calculations. For the present study, we were able to estimate the effects of including turbulence and rotation. Such mechanisms can be studied just by making use of 3D simulations, which is already an innovation on the field.

Besides being able to address new problems, we could also implement a self-consistent code for dust cooling. In order to do it self-consistently, we assumed thermal equilibrium, therefore the cooling time has to be shorter than the dynamical time. By making such assumption, the total thermal energy exchange on the gas-dust interaction was set to zero. With that, dust temperature and all other necessary rates can be calculated.

With our computational machinery well set, it was time to access the problem of fragmentation. For that, high-resolution simulations were needed, since the optic thick regime is reach for low Jeans masses ($M_{Jeans} < 10^{-2} M_{\odot}$). The correspondent Jeans mass for the point where the gas becomes optically thick can be better seen in the *Omukai plot* (Omukai et al. 2005), which is show in Figure 2.1. The important feature to be noted here is the point in the gas evolution, where it becomes optically thick ($\tau > 1$). If we consider that no further fragmentation will happen after the gas enter such regime, the required resolution on the calculations has to be approximately $M_{resolution} < 10^{-2} M_{\odot}$.

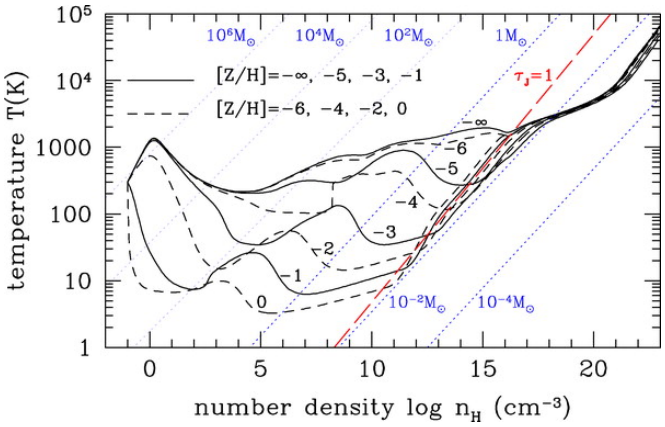

Figure 2.1: Figure taken from Omukai et al. (2005), where it shows temperature-density diagram for the evolution of pre-stellar clouds with different metallicities. The metallicities shown are $Z = 0$, 10^{-5}, 10^{-3}, and $10^{-1}Z_{\odot}$ by solid lines, and $Z = 10^{-6}$, 10^{-4}, 10^{-2}, and $1Z_{\odot}$ are shown by dashed lines. Lines of constant Jeans mass are shown in thin dotted lines. Finally, the positions at which the gas becomes optically thick is shown by the red solid line.

2.1 Resolution in SPH simulations

The resolution in SPH calculations is proportional to the mass (rather than the volume as in Eulerian grid codes) of each particle. In order to resolve self-gravitating SPH calculations, Bate & Burkert (1997) showed that the minimum Jeans mass reached in the simulations must be greater than twice the mass in an SPH kernel. An SPH kernel is made by the particle neighbors, which in our calculations correspond to approximately 50 particles on average. Therefore, the required criterion for resolving a self-gravitating SPH calculation is that the Jeans mass has to be greater than 100 SPH particles mass ($M_{Jeans} > 100 \times M_{SPH}$).

2.2 Simulations

Hereafter we present the simulations carried on the work that culminated in the first paper of the PhD period (Dopcke et al. 2011)

2.2.1 Numerical method

We model the collapse of a low-metallicity gas cloud using a modified version of the Gadget 2 (Springel 2005) smoothed particle hydrodynamics (SPH) code. To enable us to continue our simulation beyond the formation of the first very high density protostellar core, we use a sink particle approach (Bate et al. 1995b), based on the implementation of Jappsen et al. (2005). Sink particles are created once the SPH particles are bound, collapsing, and within an accretion radius, h_{acc}, which is taken to be 1.0 AU. The threshold number density for sink particle creation is $5.0 \times 10^{13}\mathrm{cm}^{-3}$. At the threshold density, the Jeans length at the minimum temperature reached by the gas is approximately one AU, while at higher densities the gas becomes optically thick and begins to heat up. Further fragmentation on scales smaller than the sink particle scale is therefore unlikely to occur. For further discussion see Clark et al. (2011a).

To treat the chemistry and thermal balance of the gas, we use the same approach as in Clark et al. (2011a), with two additions: the inclusion of the effects of dust cooling, as described below, and formation of H2 on the surface of dust grains (see Hollenbach & McKee 1979). The Clark et al. (2011a) chemical network and cooling function were designed for treating primordial gas and do not include the chemistry of metals such as carbon or oxygen, or the effects of cooling from these atoms, or molecules containing them such as CO or H_2O. We justify this approximation by noting that previous studies of very low-metallicity gas (e.g. Omukai et al. 2005, 2010) find that gas-phase metals have little influence on the thermal state of the gas. Omukai et al. (2010) showed that H2O and OH are efficient coolants at $10^8 < n < 10^{10}\mathrm{cm}^{-3}$ for their one-zone model. In their hydrodynamical calculations, however, the collapse is faster, and the effect of H2O and OH is not perceptible. Therefore we do not expect oxygen-bearing molecules to have a big effect on the thermal evolution of the gas. For the metallicities and dust-to-gas ratios considered in this study, the dominant sources of cooling are the standard primordial coolants (H_2 bound-bound emission and collision-induced emission) and energy transfer from the gas to the dust.

Dust cooling

Collisions between gas particles and dust grains can transfer energy from the gas to the dust (if the gas temperature T is greater than the dust temperature $T_{\rm gr}$), or from the dust to the gas (if $T_{\rm gr} > T$). The rate at which energy is transferred from gas to dust is given by (Hollenbach & McKee 1979)

$$\Lambda_{\rm gr} = n_{\rm gr} n \bar{\sigma}_{\rm gr} v_{\rm p} f(2kT - 2kT_{\rm gr}) \ \mathrm{erg\,s^{-1}\,cm^{-3}}, \tag{2.1}$$

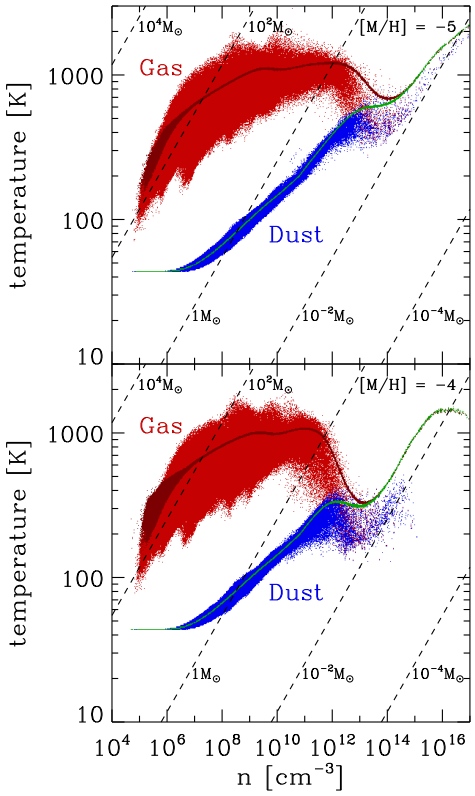

Figure 2.2: Results of our low-resolution simulations, showing the dependence of gas and dust temperatures on gas density for metallicities 10^{-4} and 10^{-5} times the solar value. In red, we show the gas temperature, and in blue the dust temperature for the turbulent and rotating cloud. The simple core collapse is overploted in dark red and green. The points with thinner features are from the simulations without rotation or turbulence, while those showing more scatter come from the simulations with rotation and turbulence. The dashed lines show constant Jeans mass values.

where $n_{\rm gr}$ is the number density of dust grains, n is the number density of hydrogen nuclei, $\bar{\sigma}_{\rm gr}$ is the mean dust grain cross-section, $v_{\rm p}$ is the thermal speed of the proton, and f is a factor accounting for the ontribution of species other than protons, as well as for charge and accommodation effects. We assume that $\bar{\sigma}_{\rm gr}$ is the same as for Milky Way dust, and that the number density of dust grains is a factor $\rm Z/Z_{\odot}$ smaller than the Milky Way value. To compute the rate at which the dust grains radiate away energy, we use the approximation (Stamatellos et al. 2007)

$$\Lambda_{\rm rad} = 4\sigma_{\rm sb} n_{\rm gr} \frac{(T_{\rm gr}^4 - T_{\rm cmb}^4)}{\Sigma^2 \kappa_R + \kappa_P^{-1}}, \tag{2.2}$$

where $T_{\rm cmb}$ is the CMB temperature, $\sigma_{\rm sb}$ is the Stefan-Boltzmann constant, κ_P and κ_R are the Planck and Rosseland mean opacities and Σ is the column density of gas measured along a radial ray from the particle to the edge of the cloud.

As explained by Stamatellos et al. (2007), this expression has the correct behaviour in the optically thin and optically thick limits, and interpolates between these two limits in a smooth fashion. In practice, we approximate further by assuming that the Planck and Rosseland mean opacities are equaland by using the fact that $\Sigma \sim \rho L_{\rm J}$ for a gravitationally collapsing gas, where ρ is the mass density of the gas, and $L_{\rm J}$ is the Jeans length, given by $L_{\rm J} = (\pi c_s^2 / G\rho)^{1/2}$, where c_s is the speed of sound in the gas. By approximating Σ in this fashion, we avoid the computational difficulties involved with measuring column densities directly in the simulation, while still following the behaviour of the gas reasonably accurately in the optically thick regime. In any case, most of the interesting behaviour that we find in our simulations occurs while dust cooling remains in the optically thin regime. To compute the temperature of the dust grains, we assume that the dust is in thermal equilibrium, and hence solve the equilibrium equation

$$\Lambda_{\rm gr} - \Lambda_{\rm rad} = 0. \tag{2.3}$$

This equation is transcendental, so we solve it numerically.

Dust opacity

We follow the dust opacity model of Goldsmith (2001), and we calculate the opacity as a function of the dust temperature in the same fashion as in Banerjee et al. (2006). To convert from the frequency-dependent opacity given in Goldsmith (2001) to our desired temperature-dependent mean opacity, we assume that for dust with temperature $T_{\rm gr}$, the dominant contribution to the

mean opacity comes from frequencies close to a frequency $\bar{\nu}$ that is given by $h\bar{\nu} = \alpha k T_{\rm gr}$, where $\alpha = 2.70$. At a reference temperature $T_0 = 6.75$ K, this procedure yields an opacity

$$\begin{aligned} \kappa(T_0) = & \ 3.3 \times 10^{-26} \alpha ({\rm n}/2\rho_{\rm gas}) \\ = & \ 2.664 \times 10^{-2}/(1 + 4[{\rm He}]) \end{aligned} \tag{2.4}$$

where [He] is the helium abundance, and n is the number density of hydrogen nuclei. At other temperatures, $\kappa \propto T_{\rm gr}^2$, so long as $T_{\rm gr} < 200$ K. For grain temperatures larger than 200 K, it is necessary to account for the effects of ice-mantle evaporation, while at much higher grain temperatures, the opacity falls off extremely rapidly due to the melting of the grains. We account for these effects (see Semenov et al. 2003) and so our opacity varies with dust temperature following the relationship

$$\kappa = \kappa(T_0) \times \begin{cases} T^2 & {\rm T} < 200{\rm K} \\ T^0 & 200{\rm K} < {\rm T} < 1500{\rm K} \\ T^{-12} & {\rm T} > 1500{\rm K} \end{cases} \tag{2.5}$$

2.2.2 Setup and Initial conditions

Resolution Level	Number of Particles	Particle Mass	Turbulence	Angular Momentum
	($\times 10^6$)	(10^{-5}M$_\odot$)	($E_{\rm turb}/\lvert E_{\rm grav}\rvert$)	($E_{\rm rot}/\lvert E_{\rm grav}\rvert$)
High	40	2.5	0.1	0.02
Low	4	25.0	0.1	0.02
			0.0	0.00

Table 2.1: Simulation properties.

We performed three sets of simulations, two at low resolution and one at high resolution. The details are shown in Table 2.1. Our low resolution simulations were performed to explore the thermal evolution of the gas during the collapse, and had 4 million SPH particles which was insufficient to fully resolve fragmentation. We used these simulations to model the collapse of an initially uniform gas cloud with an initial number density of $10^5\,{\rm cm}^{-3}$ and an initial temperature of 300 K. We modelled two different metallicities (10^{-4}Z$_\odot$ and 10^{-5}Z$_\odot$). The initial cloud mass was 1000 M$_\odot$, and the mass resolution was 25×10^{-3} M$_\odot$. In one set of low-resolution simulations the gas was initially at rest, while in the other, we included small amounts of turbulent

and rotational energy, with $E_{\rm turb}/|E_{\rm grav}| = 0.1$ and $\beta = E_{\rm rot}/|E_{\rm grav}| = 0.02$, where $E_{\rm grav}$ is the gravitational potential energy, $E_{\rm turb}$ is the turbulent kinetic energy and $E_{\rm rot}$ is the rotational energy. For our high resolution simulations, which were designed to investigate whether the gas would fragment, we employed 40 million SPH particles. We adopted initial conditions similar to those in the low-resolution run with turbulence and rotation. Again, we simulated two metallicities, $10^{-4}{\rm Z}_{\odot}$ and $10^{-5}{\rm Z}_{\odot}$. The mass resolution (taken to be 100 times the SPH particle mass) was $2.5 \times 10^{-3}{\rm M}_{\odot}$.

2.3 3D, turbulence, rotation, and self-consistent dust cooling

The calculations performed here were the first ones to address the problem of fragmentation at low-metallicities, and make use of self-consistent dust cooling calculations. When this problem is studied using 1-zone models, it is possible to solve for more chemical species. In 3D however, the calculations can become forbiddingly expensive and hard to implement, and those are reasons why previous works did not combine 3D calculations and a self-consistent chemical model.

Other important effects can be studied when the calculations are done in 3D, such as turbulence and rotation. Their effects become clear when we compare simulations with and without such feature in Figure 2.2. The thinner lines represent the simulations without additional velocities. The gas which is subjected to such velocities takes longer to collapse, therefore the PdV heating is decreased. The net effect is that the gas is on average cooler. This effect is stronger for higher densities, when the gas should have experienced more heating, in the non-turbulent gas.

Moreover, colder the gas, lower the Jeans mass. This changes the characteristic fragment mass to lower values. Simulations that include turbulence and rotation are expected to create clusters with a mass spectrum favoring low-mass objects.

2.4 Numerical solutions for the temperature calculation during the collapse

In order to get a good estimation of the gas temperature during the collapse, we also needed to have accurate dust temperatures, and dust cooling rates. The most influential factor on that is the dust opacity. This opacity will

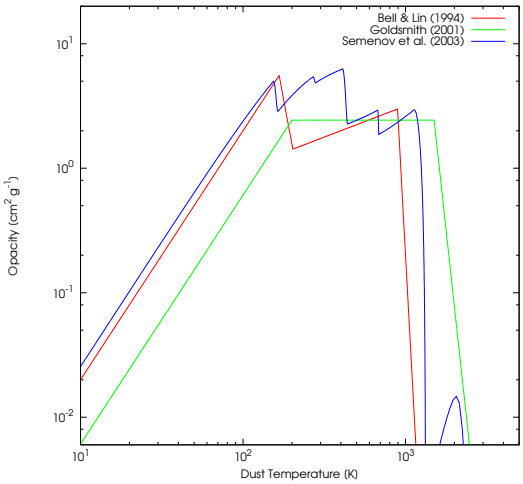

Figure 2.3: Comparison of dust opacities dependence with temperature for three different models (Bell & Lin 1994; Goldsmith 2001; Semenov et al. 2003).

be included in the thermal balance calculation (Equation 2.3), and different models can result in different thermal evolutions. The effect of changing the opacity model for dust was studied, and three models were used (Figure 2.3).

Bell & Lin (1994) models the opacity dependance with density and temperature in the form:

$$\kappa = \kappa_i \rho^a T^b, \tag{2.6}$$

where κ is the dust opacity, ρ is the gas density, and T is the dust temperature. κ_i, a, and b are tabulated values for various dust components. These values were based on works from Lin & Papaloizou (1985) and Alexander et al. (1989).

Goldsmith (2001) used values for three GMCs studies by Goldsmith et al. (1997). The values were given as dependents on frequency, and our approach transformed them into temperature dependence as described in Section 2.2.1.

Finally, Semenov et al. (2003) model is based in a 5-layered spheres with different dust compounds. The values were calculated following dust composition model for accretion discs by Pollack et al. (1994).

For the high-resolution simulations, we used Goldsmith (2001) opacities for being more consistent with our study. We did however, the calculations using other dust opacity models. The results for a spherical collapse is shown in Figure 2.4.

Important to notice that there are few "jumps" in the dust temperature for the models from Bell & Lin (1994) and Semenov et al. (2003). Such jumps come from the fact that the equation for energy balance (Equation

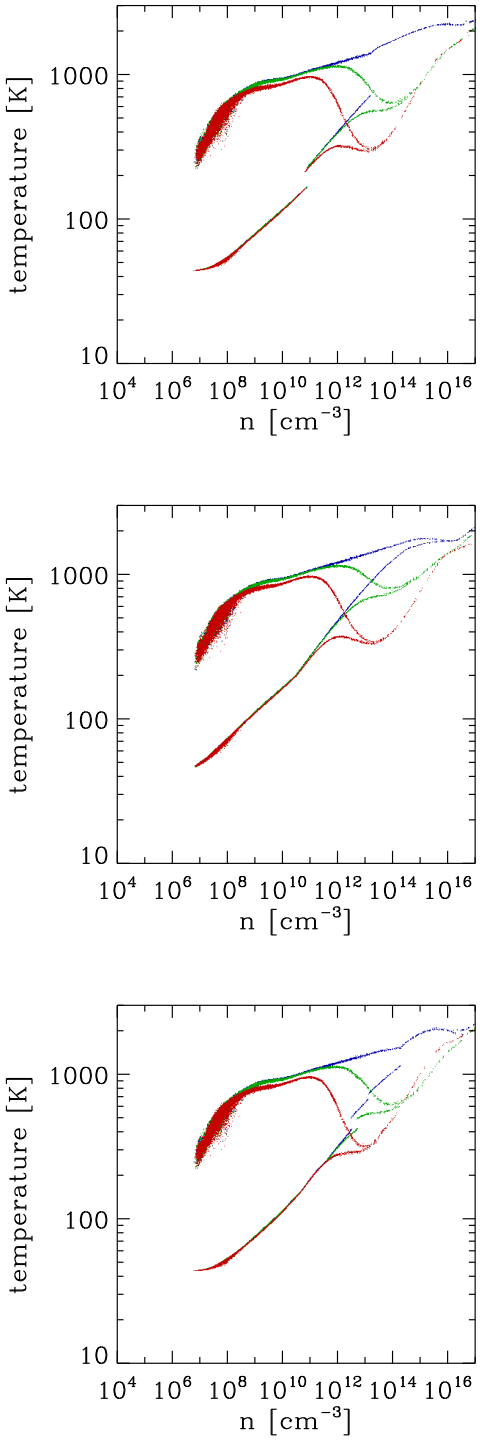

Figure 2.4: Comparison of gas and dust temperatures dependence on number density, for different dust opacity models. The panels from the top to the bottom refer to Bell & Lin (1994), Goldsmith (2001), and Semenov et al. (2003), respectively. The lines in the lower part refer to dust temperature (colder for $n < 10^{11}$ cm^{-3}), while the lines in the upper part refer to the gas temperature. The values for $Z = 10^{-4}$, 10^{-5}, and $10^{-6} Z_{\odot}$ are in red, green and blue, respectively.

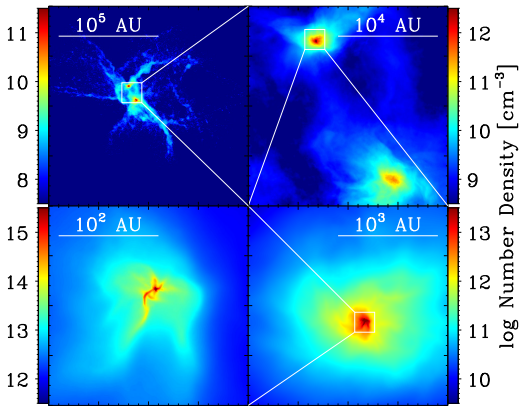

Figure 2.5: Number density maps for a slice through the high density region. The image shows a sequence of zooms in the density structure in the gas immediately before the formation of the first protostar.

2.3) has three solutions at those points. These refer to points in the collapse where some dust compounds sublimate. Now the dust is hotter, but after the sublimation, the opacity is reduced and dust becomes colder. What is happening in reality is that just part of the dust is sublimated. That is why in this picture there are more than on solution for the dust temperature. Thus the solution would be to reduce the dust density in Equation 2.1 until a single solution is recovered.

2.5 The effect of dust cooling on the IMF at low metallicity star forming clouds

2.5.1 Thermodynamical evolution of gas and dust

In Figure 2.2, we compare the evolution of the dust and gas temperatures in the low-resolution simulations. The dust temperature, shown in the lower part of the panels, varies from the CMB temperature in the low density region to the gas temperature at much higher densities.

At densities higher than 10^{11}–$10^{12}\,\mathrm{cm}^{-3}$, dust cooling starts to be effective and begins to cool the gas. The gas temperature decreases to roughly 600 K in the $10^{-5}\,\mathrm{Z}_\odot$ simulations, and 300 K in the $\mathrm{Z} = 10^{-4}\mathrm{Z}_\odot$ case.

This temperature decrease significantly increases the number of Jeans masses present in the collapsing region, making the gas unstable to fragmentation. The dust and the gas temperatures couple for densities higher then $10^{13}\mathrm{cm}^{-3}$, when the compressional heating starts to dominate again over the

dust cooling.

The subsequent evolution of the gas is close to adiabatic. If we compare the results of the runs with and without rotation and turbulence, then the most obvious difference is the much greater scatter in the $n-T$ diagram in the former case. Variations in the infall velocity lead to different fluid elements undergoing different amounts of compressional heating. The overall effect is to reduce both the infall velocity and the average compressional heating rate. This allows dust cooling to dominate at a density that is up to five times smaller than in the case without rotation or turbulence. The gas also reaches a lower temperature, cooling down to $\approx$ 200K (instead of 300K) for the Z $= 10^{-4}$Z$_{\odot}$ case, and to $\approx$ 400K (instead of 600K) for the Z $= 10^{-5}$Z$_{\odot}$ case. This behavior shows that it is essential to use 3D simulations to follow the evolution of the collapsing gas. A similar effect can be seen in Clark et al. (2011a).

If we compare our results to the calculations of Omukai et al. (2010), we find that dust cooling is considerably less effective than predicted by the one-zone models, but the agreement is better with their 1D hydrodynamical models.

We find that a metallicity of $10^{-4}Z_{\odot}$ is required to cool the gas down to 300 K, while for the same metallicity, Omukai et al. (2010) find that the gas cools down to 200 K.

2.5.2 Fragmentation

We follow the thermodynamical evolution of the gas up to very high densities of order 10^{17}cm^{-3}, where the Jeans mass is $\approx 10^{-2}$M$_{\odot}$, and so we need a high resolution simulation to study the fragmentation behaviour. The transport of angular momentum to smaller scales during the collapse leads to the formation of a dense disk-like structure, supported by rotation which then fragments into several objects.

Figure 3.4 shows the density structure in the gas immediately before the formation of the first protostar. The top-left panel shows a density slice on a scale comparable to the size of the initial gas distribution. The structure is very filamentary and there are two main overdense clumps in the center. If we zoom in on one of the clumps, we see that its internal structure is also filamentary. We can follow the collapse down to scales of the order of an AU, but at this point we reach the limit of our computational approach: as the gas collapses further, the Courant timestep becomes very small, making it difficult to follow the further evolution of the cloud. In order to avoid this difficulty, we replace very dense, gravitationally bound, and collapsing regions by sink particles.

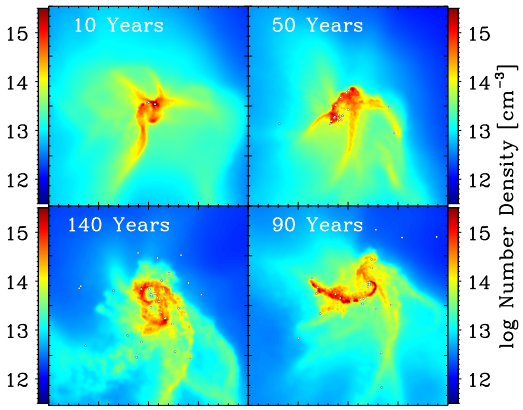

Figure 2.6: Number density map showing a slice in the densest clump, and the sink formation time evolution, for the 40 million particles simulation, and $Z = 10^{-4}Z_{\odot}$. The box is 100AU x 100AU and the time is measured from the formation of the first sink particle.

Once the conditions for sink particle creation are met, they start to form in the highest density regions (Figure 3.6). Due to interactions with other sink particles that result in an increase in velocity, some sink particles can be ejected from the high-density region, but most of the particles still remain within the dense gas. Within 137 years of the formation of the first sink particle, 45 sink particles have formed. At this time, approximately $4.6M_{\odot}$ of gas has been accreted by the sink particles.

2.5.3 Properties of the fragments

Figure 3.7 shows the mass distribution of sink particles when we stop the calculation. We typically find masses below $1M_{\odot}$, with somewhat smaller values in the $10^{-4}Z_{\odot}$ case compared to the $10^{-5}Z_{\odot}$ case. Both histograms have the lowest sink particle mass well above the resolution limit of $0.0025M_{\odot}$. Note that in both cases, we are still looking at the very early stages of star cluster evolution. As a consequence, the sink particle masses in Figure 3.7 are not the same as the final protostellar masses – there are many mechanisms that will affect the mass function, such as continuing accretion, mergers between the newly formed protostars, feedback from winds, jets and luminosity accretion, etc. Nevertheless, we can speculate that the typical stellar mass is similar to what is observed for Pop II stars in the Milky Way. This suggests that the transition from high-mass primordial stars to Population II stars with mass function similar to that at the present day occurs early in the metal evolution history of the universe, at metallicities $Z_{\rm crit} < 10^{-5}Z_{\odot}$. The

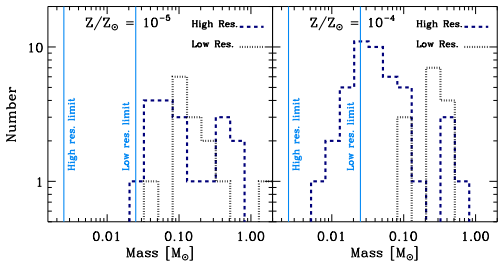

Figure 2.7: Sink particle mass function at the end of the simulations. High and low resolution results and corresponding resolution limits are shown. To resolve the fragmentation, the mass resolution should be smaller than the Jeans mass at the point in the temperature-density diagram where dust and gas couple and the compressional heating starts to dominate over the dust cooling. At the time shown, around 5 $M_\odot$ of gas had been accreted by the sink particles in each simulation.

number of protostars formed by the end of the simulation, for both $10^{-4}Z_\odot$ (45) and $10^{-5}Z_\odot$ (19) cases, is much larger than the initial number of Jeans masses (3) in the cloud.

2.6 Final considerations on this study

In this study we have addressed the question of whether dust cooling can lead to the fragmentation of low-metallicity star-forming clouds. For this purpose we performed numerical simulations to follow the thermodynamical and chemical evolution of collapsing clouds. The chemical model included a primordial chemical network together with a description of dust evolution, where the dust temperature was calculated by solving self-consistently the thermal energy equilibrium equation (Equation 2.3).

We performed three sets of simulations, two at low resolution and one at high resolution (Table 2.1). All simulations had an initial cloud mass of 1000 $M_\odot$, number density of 10^5 cm^{-3}, and temperature of 300K. We tested two different metallicities ($10^{-4}Z_\odot$ and $10^{-5}Z_\odot$), and also the inclusion of small amounts of turbulent and rotational energies.
We found in all simulations that dust can effectively cool the gas, for number densities higher than 10^{11}cm^{-3}. An increase in metallicity implies a higher dust-to-gas ratio, and consequently stronger cooling by dust. This is reflected in a lower temperature of the dense gas in the higher metallicity simulation.

For the low resolution case, we tested the effect of adding turbulence and rotation. These diminish the infall velocity, leading to different fluid elements

undergoing different amounts of compressional heating. This lack of heating allows the gas to reach a lower temperature.
We found that the transport of angular momentum to smaller scales lead to the formation of a disk-like structure, which then fragmented into a number of low mass objects.

We conclude that the dust is already an efficient coolant even at metallicities as low as 10^{-5} or $10^{-4} Z_{\odot}$, in agreement with previous works (Clark et al. 2008; Omukai et al. 2010; Schneider et al. 2002, 2006; Tsuribe & Omukai 2006, 2008). Our results support the idea that dust cooling can play an important role in the fragmentation of molecular clouds and the evolution of the stellar IMF.

2.7 What about metal free clouds?

So far, we could observe that clouds with very low metallicity can fragment and form low mass stars. At this point in our study, metal-free clouds were believed to form only very massive stars and the questions was in which point in metallicity, clouds would start to fragment and form low-mass objects. An striking work changed the picture however. Clark et al. (2011a) showed that even at zero metallicity, clouds can fragment.

Now the idea of a transition from no fragmentation at zero metallicity, and some fragmentation for a small amount of metals has faded. The question now is whether the fragmentation behavior varies at such low metallicities. Thus, the follow up of this work will be to carry simulations of metal free clouds as well as $Z = 10^{-6} Z_{\odot}$, and study the differences in the fragmentation behavior.

Chapter 3

On the physics of the low metallicity IMF

At this point of our research, new studies were done suggesting that there could be low mass Pop. III stars (Clark et al. 2011a,b; Greif et al. 2011b, 2012). This changes the picture in the sense that the change in the mode of star formation is from forming an IMF dominated by massive stars in the Pop. III case, to a IMF that tends to yield stars with masses less than the solar value. In addition to that, observational data have shown to require a "top heavy" IMF to explain the characteristics of some Galactic globular clusters (Marks et al. 2012; Kroupa et al. 2011), and also the high fraction of extremely metal-poor stars that are C-rich (Suda et al. 2012).

Furthermore, Tsuribe & Omukai (2006, 2008) and Clark et al. (2008) modeled fragmentation in very low metallicity clouds. By describing the thermal evolution of the gas using effective equations of state derived from the one-zone calculations, of Omukai et al. (2005), they showed that dust cooling can indeed foster fragmentation. Such works ignore, however, thermal inertia effects, which can yield too much fragmentation.

In Dopcke et al. (2011), we further improved upon previous treatments, by calculation dust temperature self-consistently, and thus solving the full thermal energy equation. There, we also included the effect of microwave background (CMB) heating. We found that model clouds with metallicities as low as 10^{-4} $Z_\odot$ or 10^{-5} $Z_\odot$ do indeed show evidence for dust cooling and fragmentation, supporting the predictions of Tsuribe & Omukai (2006, 2008) and Clark et al. (2008).

3.1 Extending previous calculations to an wider range of metallicities

In this part of our study, we simulate the evolution of star-forming clouds for a wider range of metallicities (10^{-4}, 10^{-5}, 10^{-6} $Z_{\odot}$, and 0), and study the effect that this has on the mass function of the fragments that form. We also investigate how properties such as cooling and heating rates, and number of Bonnor-Ebert masses (Bonnor 1956; Ebert 1955) of the fragmenting clouds vary with metallicity and whether there is any systematic change in behavior with increasing metallicity.

3.2 Simulations

3.2.1 Numerical method

The calculations shown in this work are aimed to model the collapse of very low-metallicity clouds. For that, we make use of a modified version of the Gadget 2 (Springel 2005) smoothed particle hydrodynamics (SPH) code. In order to advance the calculations later in the collapse, when densities become very high, we make use of the sink particle approach (Bate et al. 1995b; Jappsen et al. 2005). This enables us to go beyond the formation of the first contracting protostar.

This sink particles are created when a minimum of 100 sink particles are bound, collapsing, and within an accretion radius, h_{acc}, which we take to be 1.0 AU. We set the threshold number density for sink particle creation is $5.0 \times 10^{15}\mathrm{cm}^{-3}$, which is reached when the gas becomes optically thick and further fragmentation is unlikely. For further discussion of the details of our sink particle treatment, we refer the reader to Clark et al. (2011b).

As discussed e.g. by Omukai et al. (2005, 2010), the gas becomes optically thick at densities around 10^{15} cm^{-3}. Beyond this value, further fragmentation is strongly suppressed and our choice of sink particle formation threshold ensures that single sink particles represent individual protostars rather then groups of objects (see also the discussion by Greif et al. 2012).

Furthermore, SPH with the smoothing we employ (i.e. the standard SPH cubic spline smoothing) prevents fragmentation below the resolution limit. As shown by many works (Bate & Burkert 1997; Whitworth 1998; Hubber et al. 2006), SPH does not suffer from artificial fragmentation, at the resolution limit if gravitational forces and pressure gradients are resolved equally well.

We assume that the mean dust grain cross section is the same as for

Milky Way dust and that the number density of dust grains is a factor $Z/Z_\odot$ smaller than the Milky Way value (see Dopcke et al. 2011). To treat the chemistry and thermal balance of the gas, we use the same approach as in Clark et al. (2011b), with the inclusion of dust cooling. The Clark et al. (2011b) chemical network and cooling function were designed for treating primordial gas and do not include the chemistry of metals such as carbon or oxygen, or the effects of cooling from these atoms, or molecules containing them such as CO or H_2O. We justify this approximation by noting that previous studies of very low-metallicity gas (e.g. Omukai et al. 2005, 2010) find that gas-phase metals have little influence on the thermal state of the gas. Omukai et al. (2010) showed that H_2O and OH are efficient coolants at $10^8 < n < 10^{10}\mathrm{cm}^{-3}$ for their one-zone model. In their hydrodynamical calculations, however, the collapse is faster, and the effect of H_2O and OH is not perceptible. Therefore we do not expect oxygen-bearing molecules to have a noticeable effect on the thermal evolution of the gas.

For the metallicities and dust-to-gas ratios considered in this study, the dominant sources of cooling are the standard primordial coolants (H_2 bound-bound emission and collision-induced emission) and energy transfer from the gas to the dust.

Collisions between gas particles and dust grains can transfer energy from the gas to the dust (if the gas temperature T is greater than the dust temperature $T_{\rm gr}$), or from the dust to the gas (if $T_{\rm gr} > T$). Full details of the dust cooling treatment can be found in Dopcke et al. (2011).

3.2.2 Setup and Initial conditions

We performed a set of four simulations, with metallicities $Z/Z_\odot = 10^{-4}$, 10^{-5}, 10^{-6}, and the metal-free case. Each simulation used 40 million SPH particles, and the total mass of the cloud was $1000\,M_\odot$. The initial number density was taken to be $10^5\ \mathrm{cm}^{-3}$ and an initial temperature of 300 K. We also included small amounts of rotational and turbulent energy, which were taken to be 2% for rotation and 10% for turbulence, when compared to the gravitational potential energy.

The mass resolution is $2.5 \times 10^{-3} M_\odot$, which corresponds to 100 times the SPH particle mass (see e.g. Bate & Burkert 1997). The redshift chosen was $z = 15$, when the cosmic microwave background temperature was 43.6K. The dust properties were taken from Goldsmith (2001), and the dust grain opacities were calculated in the same fashion as in Banerjee et al. (2006). In the calculations, the opacities vary linearly with Z, which means for instance that for the $Z/Z_\odot = 10^{-4}$ calculations, the opacities were 10^{-4} times the original values.

3.3 Details of the thermal physics during the collapse

Dust cooling is a consequence of inelastic gas-grain collisions, and thus the energy transfer from gas to dust vanishes when they have the same temperature. We therefore expect the cooling to cease when the dust reaches the gas temperature. In order to evaluate the effect of dust on the thermodynamic evolution of the gas and verify this assumption, we plot in Figure 3.2, the temperature and density for the various metallicities tested. We compare the evolution of the dust and gas temperatures in the simulations, at the point of time just before the formation of the first sink particle (see Table 3.1). The dust temperature (shown in blue) varies from the CMB temperature in the low density region to the gas temperature (shown in red) at much higher densities.

After the gas reaches very high densities (n $> 10^{15}$ g cm^{-3}), the collapse is hold by thermal and rotational energies. In order to predict the fragmentation behavior, we compare thermal and rotational energies with gravitational energy in Figure 3.1.

We show the fraction of thermal energy compared to gravitational energy ($\alpha \equiv E_{thermal}/E_{grav}$) in the bottom panel of Figure 3.1. This fraction is closely related to the evolution shown in Figure 3.3, which indicates that T is higher for lower Z at the point where the gas fragments. The amount of enclosed mass at the point where $E_{thermal}$ balances E_{grav} ($\alpha = 1.0$) varies with Z. The highest value is $\sim 0.035 M_{\odot}$ for Z = 0, and the lowest is $\sim 0.0065 M_{\odot}$ for Z = 10^{-4} Z$_{\odot}$.

When we compare rotational with gravitational energy ($\beta \equiv E_{rot}/E_{grav}$), we observe that the balance is reached at M$_{enc} \approx 0.015 M_{\odot}$ for Z = 10^{-6} Z$_{\odot}$, and one third of this value for the other Z.

The more interesting value for the enclosed mass is found when we take into account both E_{rot} and $E_{thermal}$ to balance E_{grav}. The enclosed mass when $\alpha + \beta = 1$ represents the smallest value for a fragment in this type of analysis. A comparison with the sink particles that formed later is shown in Table 3.1.

Changes in metallicity influence the density at which dust cooling becomes efficient. For the Z = 10^{-4} Z$_{\odot}$ case, dust cooling begins to be efficient at $n \approx 10^{11}$cm^{-3}, while for Z = 10^{-5} Z$_{\odot}$, the density where dust cooling becomes efficient increases to $n \approx 10^{13}$cm^{-3}. For the Z = 10^{-6} Z$_{\odot}$ case, dust cooling becomes important for $n \gtrsim 3 \times 10^{13}$ cm^{-3}, preventing the gas temperature from exceeding 1500 K. For comparison, in the metal-free case the gas reaches temperatures of approximately 2000 K.

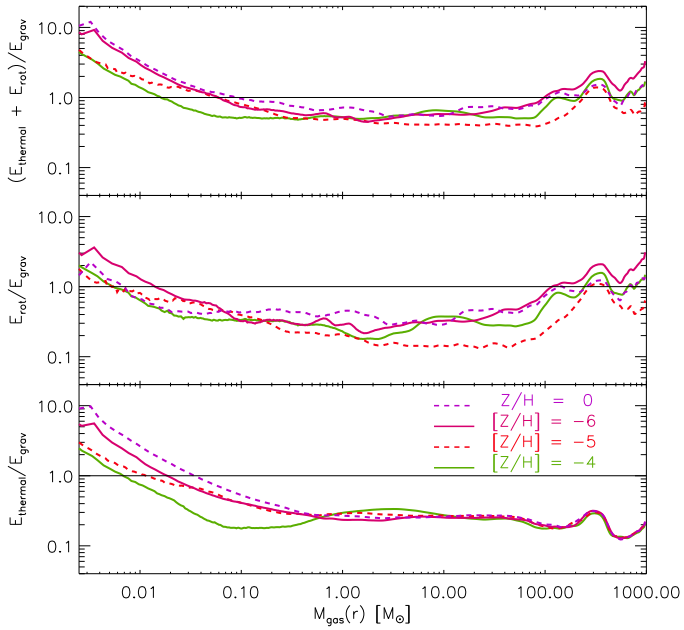

Figure 3.1: Comparison between thermal, rotational and gravitational energies *versus* enclosed gas mass, for different Z. The values were calculated just before the first sink was formed. The horizontal lines in the center of each panel indicate when rotational, thermal, or both balance the gravitational energy.

The efficiency of the cooling is also expressed in the temperature drop at high densities. The gas temperature decreases to roughly 400 K in the 10^{-5} $Z_\odot$ simulation, and 200 K in the $Z = 10^{-4}$ $Z_\odot$ case. This temperature drop significantly increases the number of Jeans masses present in the collapsing region, making the gas unstable to fragmentation. The dust and the gas temperatures couple for high densities, when the compressional heating starts to dominate again over the dust cooling. The subsequent evolution of the gas is close to adiabatic.

When we compare our results to the calculations of Omukai et al. (2010), we find good agreement with their 1D hydrodynamical models, although we expect some small difference due to effects of the turbulence and rotation (see Dopcke et al. 2011) and also due to the use of different dust opacity models.

3.4 Endless physical mechanisms that affects star formation

3.4.1 Temperature

The thermal evolution of the gas during the collapse takes different paths depending on the metallicity, as shown in the density-temperature diagram (Figure 3.2). In order to explain this behavior, we take a closer look at the cooling and heating processes involved. In Figure 3.3 we show the main cooling and heating rates divided into four panels for the different metallicities. These rates were calculated by averaging values of individual SPH particles in one density bin, where the total density range was divided in 500 bins in log space.

At densities below $n \approx 10^{10}\mathrm{cm}^{-3}$, dust cooling is unimportant in all of the runs. At these densities, the dominant coolant is H_2 line emission, while the heating is dominated by compressional (pdV) heating at $n \lesssim 10^{8}\mathrm{cm}^{-3}$, and by three body H_2 formation heating at higher densities.

At higher densities, dust cooling starts to play a more important role. In the $Z = 10^{-4}Z_\odot$ simulation, dust cooling exceeds pdV heating at $n \approx 10^{10}\mathrm{cm}^{-3}$, although it does not exceed the H_2 formation heating rate until $n \approx 10^{11}\mathrm{cm}^{-3}$. Once this occurs, and dust cooling dominates, the gas temperature drops sharply. In the $Z = 10^{-5}Z_\odot$ simulation, on the other hand, dust becomes the dominant coolant only at $n \approx 10^{13}\mathrm{cm}^{-3}$, and so the temperature decrease happens later and is smaller. Finally, in the $Z = 10^{-6}Z_\odot$ case, dust cooling becomes competitive with pdV heating only at the very end of the simulation, and so the effect on temperature evolution is less evident.

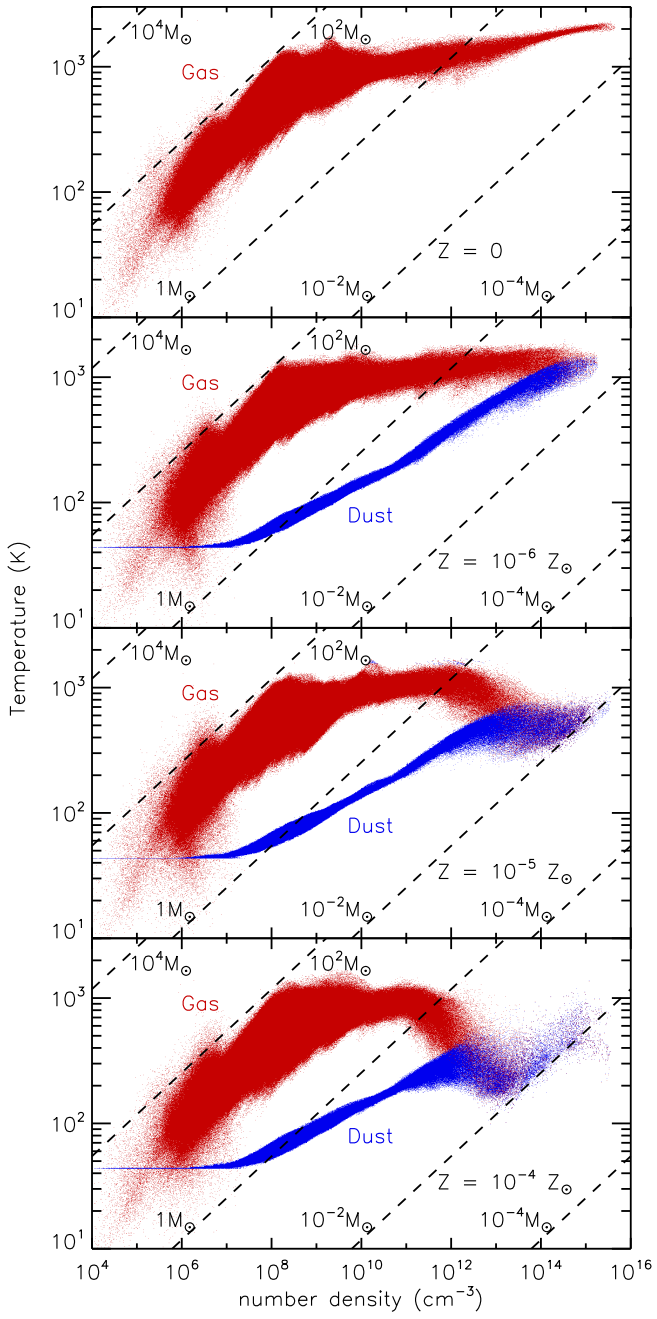

Figure 3.2: Dependence of gas and dust temperatures on gas density for metallicities 10^{-4}, 10^{-5}, and 10^{-6} and zero times the solar value, calculated just before the first sink particle was formed (see Table 3.1). In red, we show the gas temperature, and in blue the dust temperature. The dashed lines are lines of constant Jeans mass.

The other thermal processes play a minor role during the collapse. For example, H_2 dissociation cooling only becomes important in the runs with Z = $10^{-6} Z_\odot$ and 0, and only for $n > 10^{13}\mathrm{cm}^{-3}$. At very high densities ($n > 10^{14}\mathrm{cm}^{-3}$), H_2 collision-induced emission (CIE) cooling also begins to be important. For more details on H_2 heating and cooling processes in this very high density regime, we refer to Clark et al. (2011b).

3.4.2 Morphology

The transport of angular momentum to smaller scales during the collapse leads to the formation of a dense disk-like structure, supported by rotation. This disk then fragments into multiple objects.

Figure 3.4 shows the density structure of the gas immediately before the formation of the first protostar. The top-left panel shows a density slice on a scale comparable to the size of the initial gas distribution. The structure is very filamentary and there are two main over-dense clumps in the center. If we zoom in on one of the clumps, we see that its internal structure is also filamentary. Observe that at large scales the gas cloud properties are the same for all metallicities. Differences in the thermodynamic evolution appear only at $n \gtrsim 10^{11}$ cm^{-3} (see Figure 3.2). As a consequence, we observe variations in the cloud structure only in the high-density regions.

Once the conditions for sink particle creation are met (see Section 3.2.1), they start to form in the highest density regions (Figure 3.6). Then, a disk is built up in these regions, where fragmentation also occurs (Tohline 1980). During further collapse, this dense region creates spiral structures. For Z = 10^{-5} $Z_\odot$ and 10^{-4} $Z_\odot$, density waves build up spiral structures, which become locally gravitationally unstable and go into collapse. The formation of binary systems by triple encounters (Binney & Tremaine 2008) transfers kinetic energy to some sink particles, causing them to be ejected from the high density region. For Z = 10^{-5} $Z_\odot$, when the star formation efficiency (SFE) is 0.5%, fragmentation has already occurred in a secondary dense center, at a distance of $\sim$ 20 AU from the first dense region.

For Z = 10^{-6} $Z_\odot$ and 0, the formation of spiral structures is not observed. In these two runs, star formation occurs mainly in the central clump.

3.4.3 Instability to gravitational collapse

One way to study the effect of dust cooling on the fragmentation behavior and the final stellar IMF is to look at the changes in the number of Bonnor-Ebert (M_{BE}) masses contained in this central dense region. Using the definition from Bromm et al. (2009),

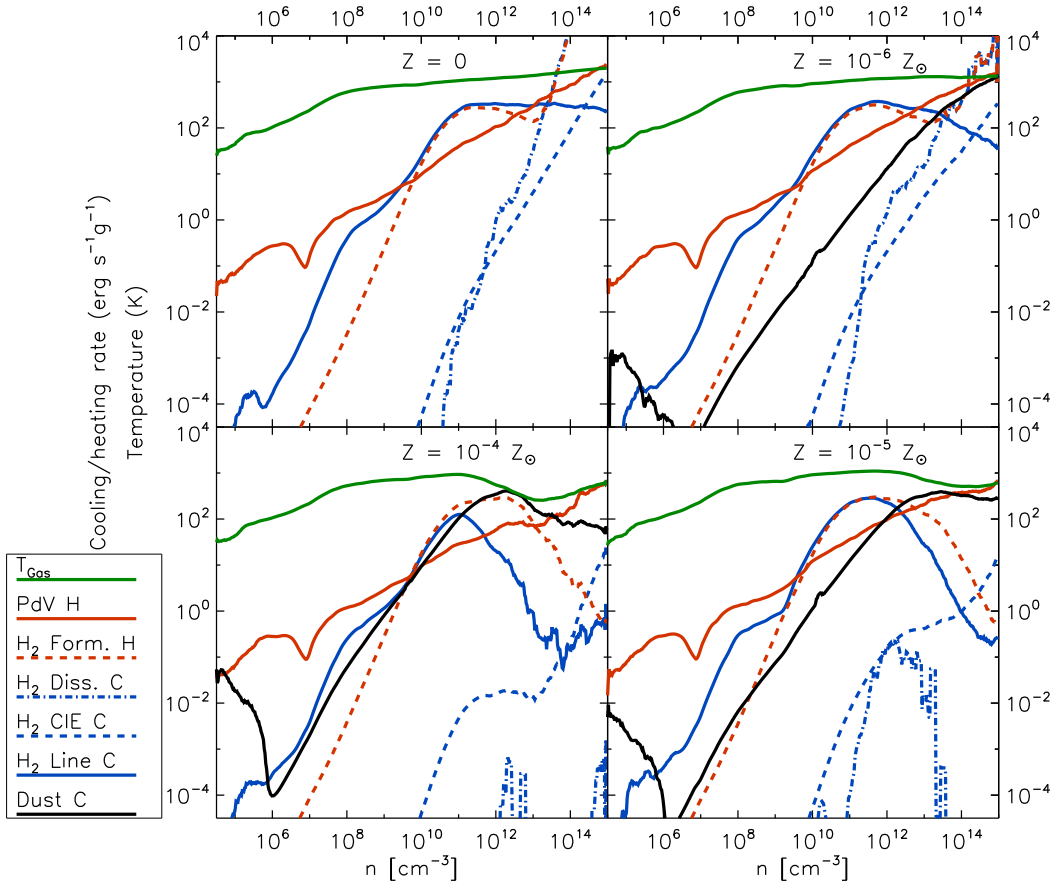

Figure 3.3: Cooling and heating rates *versus* number density for Z = 10^{-4}, 10^{-5}, 10^{-6} $Z_{\odot}$, and zero. The values are calculated just before the first sink formed. The lines labeled as "C" indicate cooling, and "H" is heating. "Dust C", "H_2 Line C", "H_2 CIE" , and "H_2 Diss." indicate dust grain cooling, H_2 line emission, collision-induced emission, and dissociation cooling, respectively. "H_2 Form. H" and "pdV H" are the H_2 formation heating rate, and compressive (pdV) heating rate.

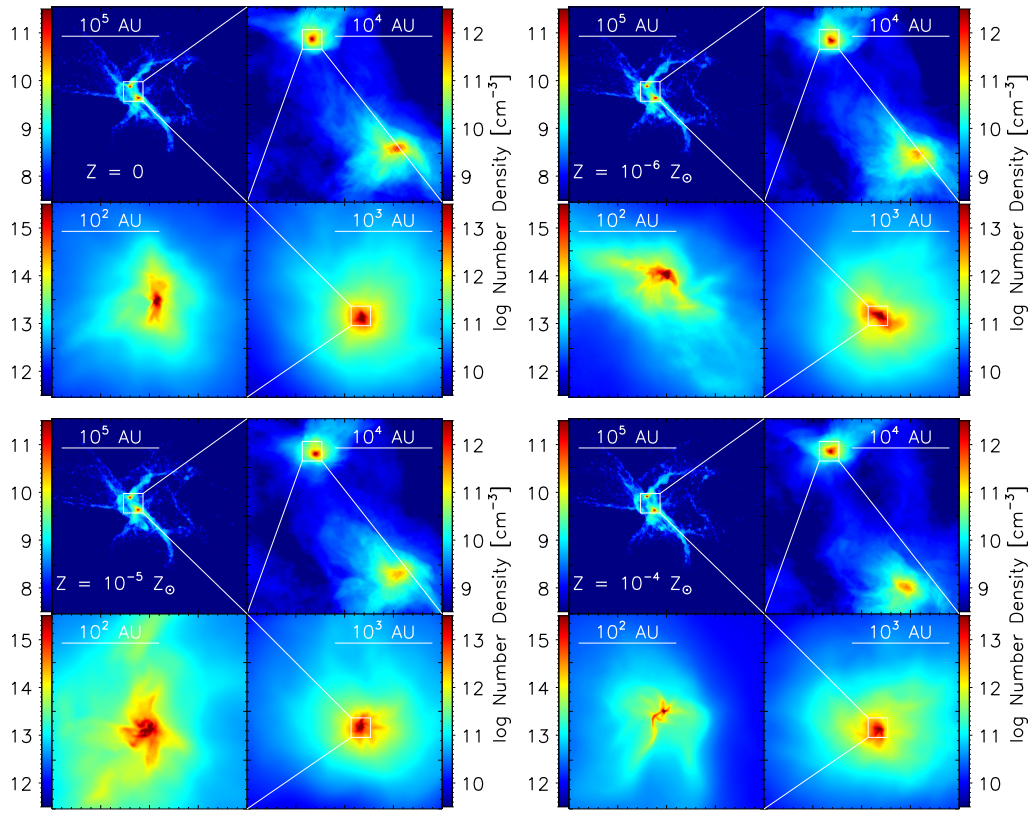

Figure 3.4: Number density maps for a slice through the high density region for Z = 10^{-4} $Z_\odot$ (top), 10^{-5} $Z_\odot$, 10^{-6} $Z_\odot$, and 0 (bottom). The image shows a sequence of zooms in on the density structure in the gas immediately before the formation of the first protostar.

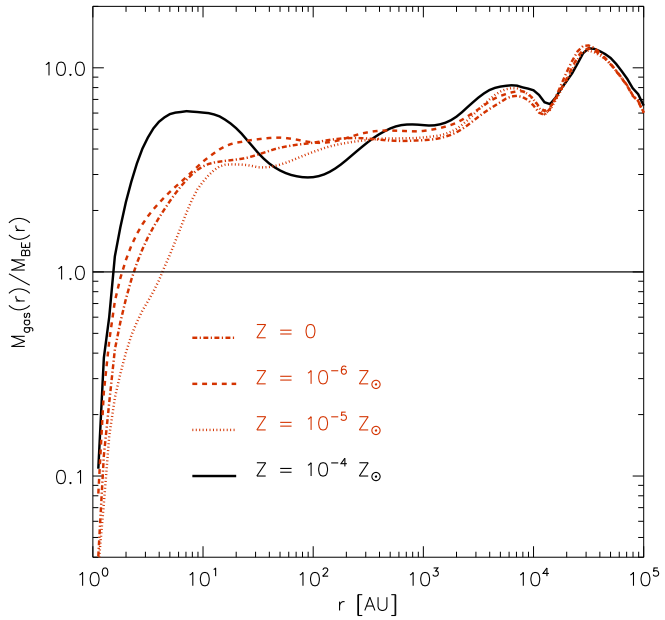

Figure 3.5: Enclosed gas mass divided by Bonnor-Ebert mass *versus* radius for different metallicities. The values were calculated at the time just before the first sink was formed and the center is taken to be the position of the densest SPH particle.

$[Z/Z_\odot]$	ST (10^3yr)	FT (yr)	SFR ($M_\odot$/yr)	$M_{enc}(\alpha\beta_1)$ ($M_\odot$)	Mean ($M_\odot$)	Median ($M_\odot$)	N
0	171.6	73	0.064	0.09	0.24	0.12	19
10^{-6}	171.2	72	0.065	0.06	0.29	0.06	16
10^{-5}	170.8	88	0.053	0.06	0.24	0.11	19
10^{-4}	169.2	138	0.034	0.02	0.10	0.05	45

Table 3.1: Sink particle properties for the different Z at the point where 4.7 $M_\odot$ are accreted in the sinks. "ST" (start time) is the time when sink particles start to form. "FT" (formation time), is the time taken to accrete 4.7 $M_\odot$ in the sinks. "SFR" is the mean star formation rate. $M_{enc}(\alpha\beta_1)$ is the enclosed mass for $\alpha + \beta = 1$ (before sinks start to form, see section 3.4.4 and Figure 3.5). Mean and median are the final mean and median sink mass. And "N" is the number of sink particles.

$$M_{BE} = 500 M_\odot \left(\frac{T}{200\mathrm{K}}\right)^{3/2} \left(\frac{n}{10^4 \mathrm{cm}^{-3}}\right)^{-1/2}, \tag{3.1}$$

for an atomic gas with temperature T and number density n, we have computed the number of Bonnor-Ebert masses contained within a series of concentric radial spheres centered on the densest point in each of our four simulations. The results are shown in Figure 3.5.

At the beginning of the simulation, the cloud had ~ 3 M_{BE}. During the collapse, the gas cools and reaches ~ 6 M_{BE} in all cases. Cooling and heating are different depending on the metallicity, and this difference is seen for distances smaller than ~ 400 AU. The $Z = 10^{-4}$ $Z_\odot$ case, for instance, has twice the number of M_{BE} for distances smaller than ~ 10 AU, when compared to the other cases. This will have direct consequences for the fragment mass function as we will see in the next section.

3.4.4 Fragmentation

The simulations were stopped at a point in time when 4.7 $M_\odot$ of gas has been accreted into the sink particles. This is sufficient to identify the two fundamental modes of fragmentation discussed in Section 3.5.

Figure 3.7 shows the mass distribution of sink particles at that time. We typically find sink masses below 1 $M_\odot$, with somewhat smaller values in the 10^{-4} $Z_\odot$ case compared to the other cases. No sharp transition in fragmentation behavior was found, but rather a smooth and complex interaction between kinematic and thermodynamic properties of the cloud.

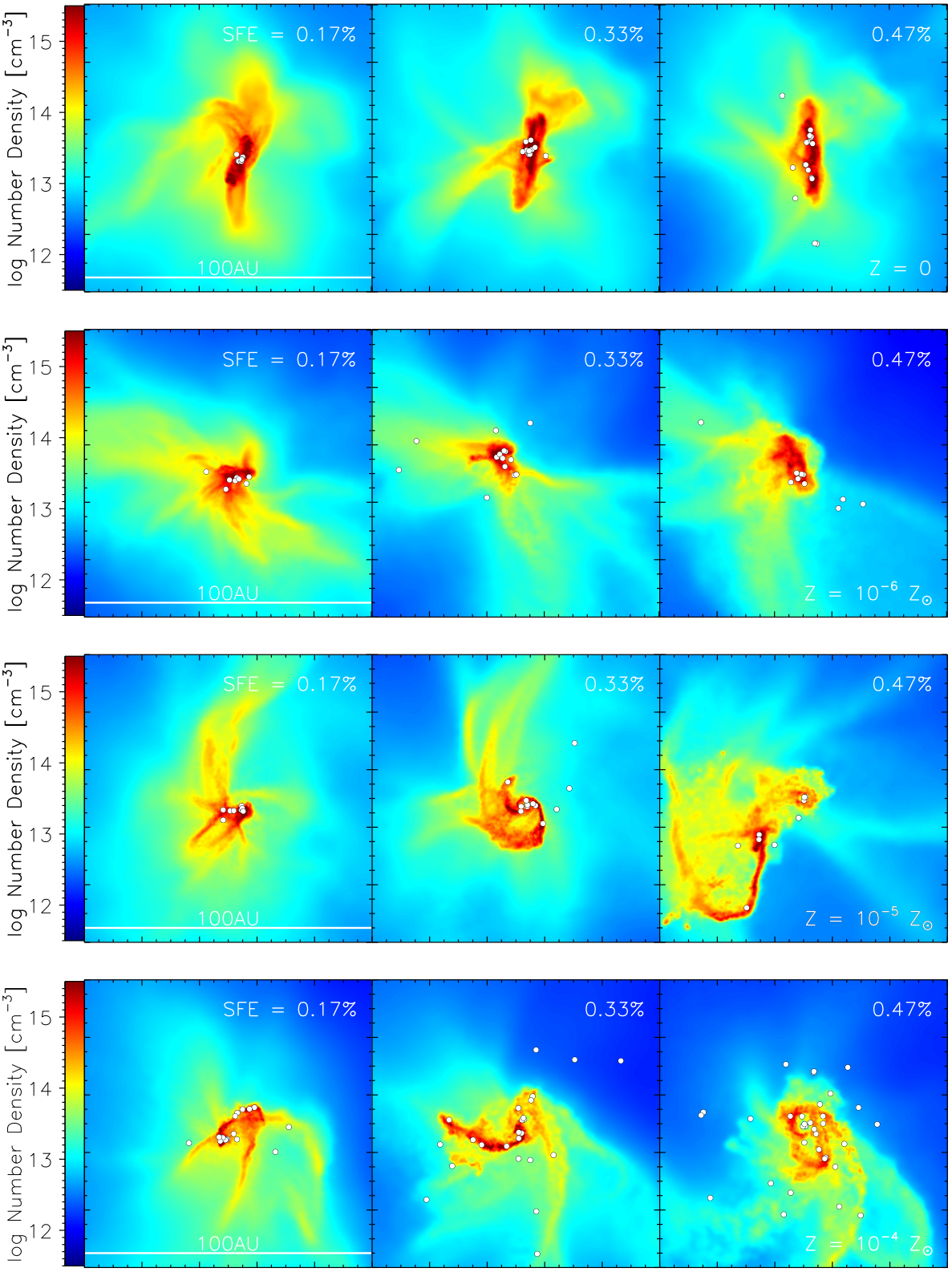

Figure 3.6: Number density map showing a slice through the densest clump, and the star formation efficiency (SFE) for Z = 10^{-4} Z$_\odot$ (bottom), 10^{-5} Z$_\odot$, 10^{-6} Z$_\odot$, and 0 (top). The box is 100AU x 100AU and the percentage indicates the star formation efficiency, i.e. the total mass in the sinks divided by the cloud mass (1000M$_\odot$).

Table 3.1 lists the main sink particle properties. It shows that the time taken to form the first sink particle is slightly shorter for higher metallicities. This shorter time is a consequence of the more efficient cooling by dust, which decreases the thermal energy that was delaying the gravitational collapse. In Table 3.1 we also observe that the star formation rate is lower for Z = 10^{-4} $Z_{\odot}$. This is because star formation started at an earlier stage of the collapse, when the mean density of the cloud was lower and there was less dense gas available to form stars.

3.4.5 Star formation rates

3.4.6 The stellar mass distribution

To better understand whether the resulting protostellar cluster was affected by varying the metallicity, we plot the final sink mass distribution in Figure 3.7. It shows that for the simulations with $Z \leq 10^{-5}$ $Z_{\odot}$, the resulting sink particle mass function is relatively flat. There are roughly equal numbers of low-mass and high-mass stars, implying that most of the mass is to be found in the high-mass objects. This mass function is consistent with those found in other recent studies of fragmentation in metal-free gas (Greif et al. 2011b; Smith et al. 2011). If the sink particle mass function provides a reliable guide to the form of the final stellar IMF, it suggests that at these metallicities, the IMF will be dominated by high-mass stars.

All of the histograms in Figure 3.7 have the lowest sink particle mass well above the resolution limit of $0.0025 M_{\odot}$. Note that in all cases, we are still looking at the very early stages of star cluster evolution. As a consequence, the sink particle masses in Figure 3.7 are not the same as the final protostellar masses – there are many mechanisms that will affect the mass function, such as continuing accretion, mergers between the newly formed protostars, feedback from winds, jets and luminosity accretion.

3.5 Timescales

One way to explain the final mass distribution of the fragments is to look at the timescales for mass accretion and fragmentation. The degree of gravitational instability inside a volume can be represented by the number of Bonnor-Ebert masses contained in this volume. We can therefore estimate the fragmentation timescale by computing the time taken for the central dense region to accrete one Bonnor-Ebert mass. In other words, we have $t_{\rm frag} \equiv {\rm M_{BE}}/\dot{\rm M}$, where $\dot{\rm M}$ is the accretion rate. This value is shown as a func-

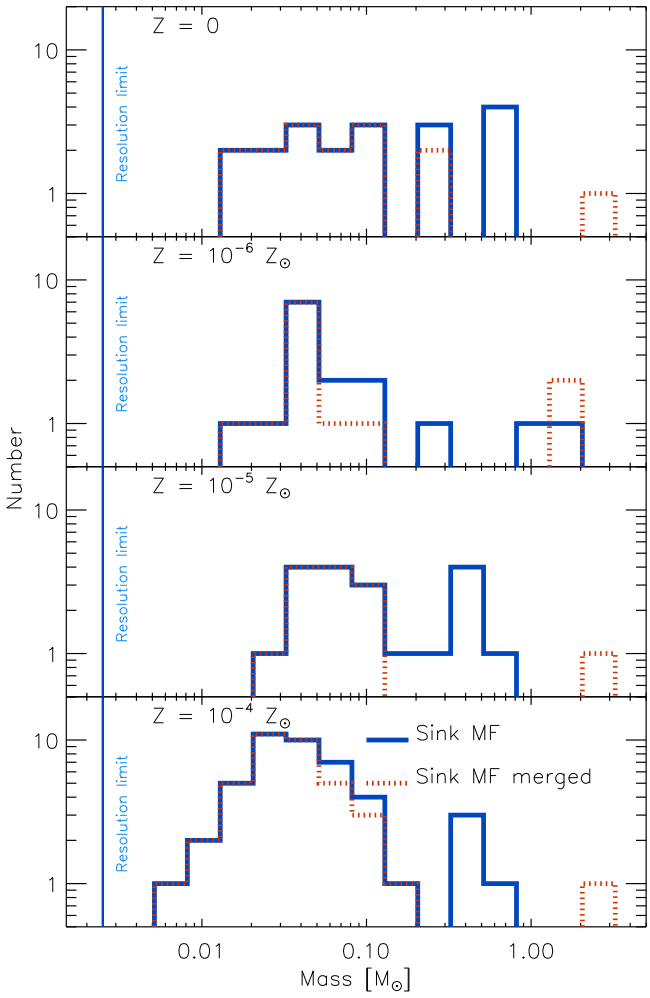

Figure 3.7: Sink particle mass function at the point when 4.7 $M_{\odot}$ of gas had been accreted by the sink particles. The mass resolution of the simulations is indicated by the vertical line. We also plot the sink mass function considering the sink particles that could have merged due to collisions (see Section 3.5.3).

tion of the enclosed gas mass in Figure 3.8, where the values are calculated for particles in spherical shells, and the center is taken to be the densest SPH particle. $\dot{M}$ is obtained by summing up the mass of the particles (m_p) inside a shell times their radial velocity (v_r), $\dot{M} \equiv \sum_{shell} m_p v_r$. This way of estimating the expected mass accretion in the sink particles is motivated by the results in Clark et al. (2011a, see Figure 3b). They demonstrate that the mass accretion rate based on the radial mass infall profile is a good estimate of that actually measured by the sink particles.

For comparison, we also plot the accretion timescale, here defined as the time taken by the gas to accrete the mass enclosed by that radius, $t_{\rm acc} \equiv {\rm M_{enc}}/\dot{\rm M}$. When the fraction $t_{\rm frag}/t_{\rm acc} > 1$, one expects that the gas enclosed by this shell is going to be accreted faster than it can fragment, favoring high-mass objects. Conversely, for $t_{\rm frag}/t_{\rm acc} < 1$, the gas will fragment faster than it can be accreted by the existing fragments, and the final mass distribution is expected to have more low-mass objects. Note that as defined here, the timescale on which new fragments form $t_{\rm frag}/t_{\rm acc}$ is the inverse of the quantity ${\rm M_{gas}}/{\rm M_{BE}}$ plotted in Figure 3.5.

In Figure 3.8, the simulation with ${\rm Z} = 10^{-4}\ {\rm Z_\odot}$ has the lowest values for $t_{\rm frag}/t_{\rm acc}$, over a wide range of $\rm M_{enc}$. This indicates that more low-mass fragments are expected to form in this case, leading to a steeper fragment mass function.

Now we can compare the predicted values before sink formation started with the final accretion and fragmentation timescales. These values are designed to represent the characteristic timescales on which the mass histogram changes: the fragmentation timescale ($\tau_{\rm frag}$) is the time on which the number of fragments change by a significant amount, while the accretion timescale ($\tau_{\rm acc}$) represents the time on which the existing fragments grow in mass. We therefore define $\tau_{\rm frag} \equiv n/\dot{n}$, and $\tau_{\rm acc} \equiv M/\dot{M}$, where n is the number of sink particles, and M is the total mass incorporated into sink particles.

Both timescales should increase over time, since the number of sink particles and the total mass also increase. This reflects the fact that it takes longer to change the shape of the mass histogram in frequency when the number of elements is higher, and in mass when the total mass is high. The key point is that these timescales are related to the shape of the histogram. If the timescale for accretion is shorter than the timescale for fragmentation, the histogram will tend to be dominated by high-mass objects. Conversely, if the fragmentation timescale is shorter than the accretion timescale, the low-mass part will be populated before the objects can grow and occupy higher mass bins. Therefore, a comparison between $\tau_{\rm acc}$ and $\tau_{\rm frag}$ helps us to understand the shape of the mass histogram.

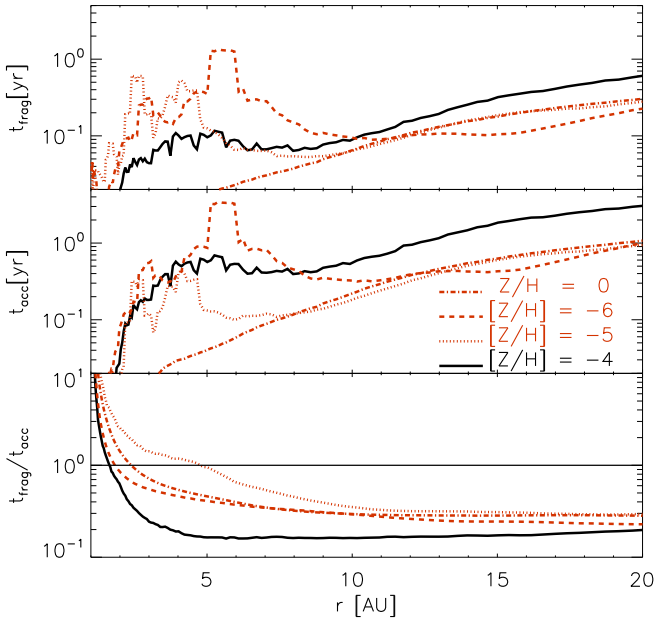

Figure 3.8: Timescales for fragmentation (top panel) and accretion (middle panel), and also their ratio (bottom panel) according to the radius for the metallicities tested. The values were calculated just before the first sink particle was formed.

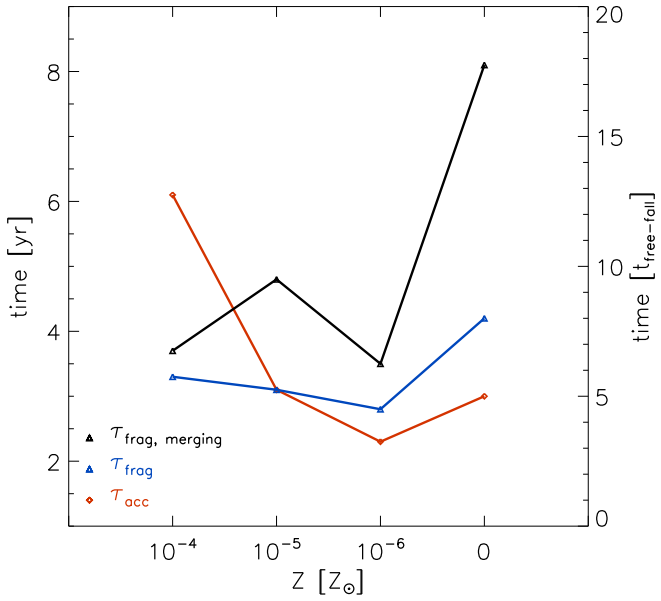

Figure 3.9: Timescales for fragmentation and accretion for different metallicities calculated for the sink particles following Equations 3.2 and 3.3. $\tau_{frag,merged}$ refers to the values considering that sink particles can merge due to collisions (see Section 3.5.3).

We calculate the average $\tau_{\rm acc}$ and $\tau_{\rm frag}$ at each point in time. The value for the mean $\tau_{\rm frag}$ and $\tau_{\rm acc}$ is calculated by the time-weighed individual times as in equations 3.2 and 3.3:

$$\tau_{\rm frag} \equiv \frac{1}{t}\sum \frac{1}{\dot{n}_i}\Delta t = \frac{1}{t}\sum \frac{t_i}{n_i}\Delta t, \tag{3.2}$$

$$\tau_{\rm acc} \equiv \frac{1}{t}\sum \frac{\langle M\rangle}{\dot{M}_i}\Delta t = \frac{1}{t}\sum \frac{t_i\,\langle M\rangle}{M_i}\Delta t, \tag{3.3}$$

where i refers to each snapshot of the simulation, and it varies from 2 to the total number of snapshots. n_i, M_i, t_i, and t are the number of sink particles, the total mass in sinks, the time at the snapshot i, and the total time of sink particle formation in each simulation, respectively. $\langle M\rangle$ is the average mass of a sink particle in the simulations including all metallicities. This average mass ($\langle M\rangle$) is used to make $\tau_{\rm acc}$ in units of time, and comparable to the accretion time. Other values were tried, such as the total average mass for each metallicity. However, the accretion time was not affected considerably. Thus, the comparison between accretion and fragmentation leads to qualitatively equal results, independent of the value used to get the correct dimension for $\tau_{\rm acc}$.

Important to notice that $\tau_{\rm frag,merging}$ is calculated in the same way as $\tau_{\rm frag}$, with the difference that the number of sink particles (n_i) is always lower or equal to the non-merging case. That is why $\tau_{\rm frag,merging}$ has higher values when compared to $\tau_{\rm frag}$.

Figure 3.9 shows the average timescales for fragmentation and accretion for different metallicities. We also plot the values considering the sink particles that could have merged due to collisions (see Section 3.5.3). These results explain the difference in the sink particle mass distribution in Figure 3.7. For $Z \leq 10^{-5}$ $Z_\odot$, the fragmentation time is always larger than the accretion time, indicating that the sink particles will accrete faster than they can be generated, resulting in a flatter mass distribution. On the other hand, when the fragmentation time is longer than the accretion time (for $Z = 10^{-4}$ $Z_\odot$), the gas fragments, rather than moving to the center and being accreted. As a consequence, the low-mass end of the protostellar mass function grows faster than the high-mass end, and the slope of the mass function steepens. This behavior agrees well with the predictions from before fragmentation started, shown in Figure 3.8.

Note that the values in Figure 3.8 were calculated before the formation of the first sink particle, while the values in Figure 3.9 were calculated using the sink particle properties. A comparison between them is useful to evaluate whether the gas cloud properties from before star formation started could be used to predict its star formation behavior. The trend in both figures is that the fragmentation timescale is normally shorter than the accretion timescales for $Z = 10^{-4}$ $Z_\odot$. From these results we conclude that the mass distribution in Figure 3.7 can be explained by the timescales in Figure 3.9, in particular the fact that the $Z \leq 10^{-5}$ $Z_\odot$ simulations have more high-mass objects. The last finding is that the transition from Pop. III to Pop. II star formation mode is not abrupt, in the sense that there is no metallicity bellow which the gas cannot fragment. The transition is rather in the stellar initial mass function, and gas clouds with $Z \lesssim 10^{-5}$ $Z_\odot$ form a more flat IMF, while gas clouds with $Z \gtrsim 10^{-4}$ $Z_\odot$ produce a cluster with more low-mass objects (see also Clark et al. 2008).

3.5.1 The gravitational potential - sinks and gas

Another property of the star-forming cloud that we observed to vary in our calculations is the spatial mass distribution. The dependence of the enclosed gas and sink mass on the distance from the center of mass is shown in Figure 3.10. The $Z = 0$ case has almost all of the sink particle mass concentrated within $r < 8$AU. The gas density for this case is also higher in this region, when compared to the other metallicities, showing that the gas and sink

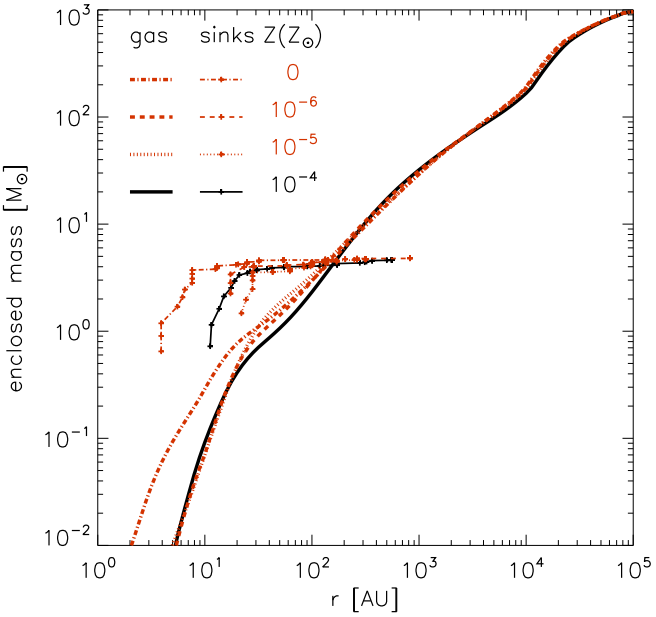

Figure 3.10: Dependence of the enclosed gas and sink mass on the distance from the center of mass, for the four simulations. The values were calculated at a point when 4.7 $M_{\odot}$ of gas had been accreted.

particle mass densities follow each other. The mass in sink particles exceeds the gas mass for small radii, being the most important component in the gravitational potential. For $r > 150$ AU, the gas becomes the most massive component, for all Z. Girichidis et al. (2012) also reported this behavior, but in their case the sink particles already started to dominate the potential below $r \approx 10^3$ AU.

This higher concentration of gas and sinks at the center occurs because for the Z = 0 case, the gas had higher temperatures in the central region. For high temperatures, the criterion for gravitational instability requires higher densities, which are achieved only very close to the center. As a consequence, the sink particle formation criteria are met just for short distances from the center.

Consequently, the dominance of sink particles mass in the gravitational potential over the gas mass, for radii smaller than 150 AU, shows the importance of treating gas and stars together in this sort of problem. It also suggests that N-body effects, such as ejections and close encounters, should play an important role in the formation of these dense star clusters, even in the very earliest stages of their evolution (see Smith et al. 2011; Greif et al. 2012).

3.5.2 Accretion

The mass accreted by the sink particles varies with the different metallicities, and affects the final sink particle mass function. It also influences the expected accretion luminosity. We did not take this process into account during our calculations, but we can estimate its importance relative to other thermal processes.

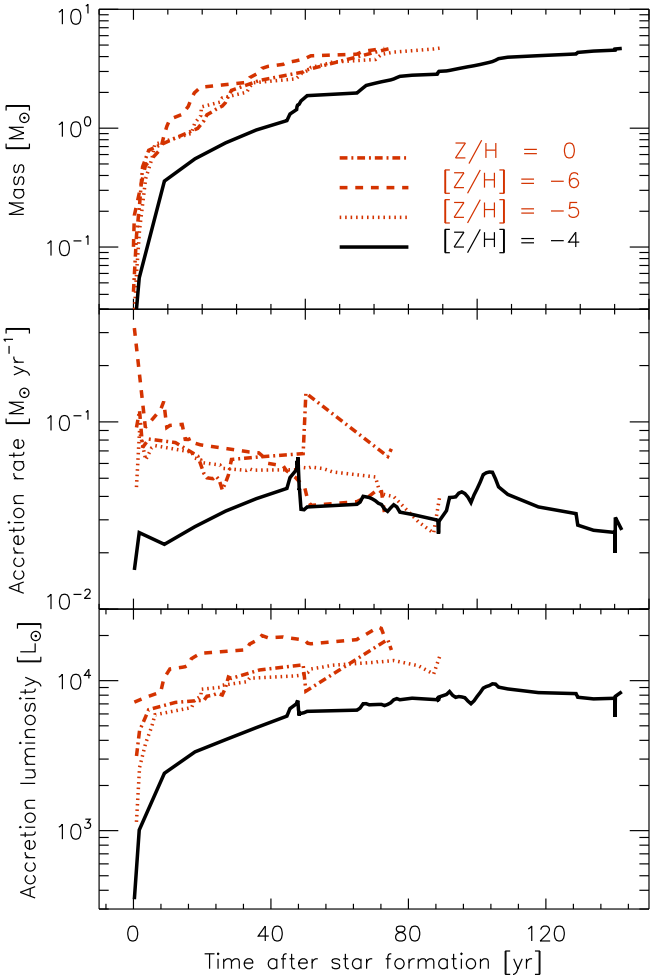

Figure 3.11: Time evolution of the mass, mass accretion rate, and accretion luminosity for the four metallicities, for all sink particles combined.

In Figure 3.11 we present the accretion properties for the newborn stellar systems. The top panel shows how the total mass in sinks evolve with time, for different metallicities. The accretion rate varies from 0.02 to 0.17 $M_\odot$ yr^{-1}, and it is on average lower for the Z = 10^{-4} Z$_\odot$ case.

In the bottom panel of Figure 3.11, we show the accretion luminosity calculated by adding up all sink particle contributions, with the standard equation,

$$L_{acc} = \frac{GM_*\dot{M}}{R_*}, \tag{3.4}$$

where $\dot{M}$ is the mass accretion rate by a protostar with mass M_*, and stellar radius R_*. We calculate R_* following Stahler et al. (1986) using

$$R_* = 66.8 \left(\frac{M_*}{M_\odot}\right)^{0.27} \left(\frac{\dot{M}}{10^{-2} M_\odot \mathrm{yr}^{-1}}\right)^{0.41} R_\odot. \tag{3.5}$$

The accretion luminosity varies from few times 10^3 $L_\odot$ to around 50×10^3 $L_\odot$, depending on metallicity. For $Z \leq 10^{-5}$ $Z_\odot$, the accretion luminosity is always over 10^4 $L_\odot$. The $Z = 10^{-4}$ $Z_\odot$ case has the lowest estimated accretion luminosity, around four times lower than the other cases. The values found for the accretion luminosity are similar to the ones found by Smith et al. (2011) for $Z = 0$, where they argue that accretion luminosity could delay the fragmentation, but not prevent it.

We can now compare this expected luminosity, and its consequent heating, to the heating processes in Figure 3.3. We make the assumption that gas and dust are absorbing the radiation in the optically thin regime. This overestimates the effects, and we obtain an upper limit for the accretion luminosity heating,

$$\Gamma_{acc} = \kappa_P \left(\frac{L_{acc}}{4\pi r^2}\right) \mathrm{erg\ s^{-1} g^{-1}} \tag{3.6}$$

where ρ_g is the gas density, κ_P is the Planck mean opacity, and r is the distance from the source. We also assume that heating occurs at $\rho \approx 10^{-9}$g cm^{-3}. With this assumption we can calculate the mean gas temperature, and use the Planck mean opacity for the gas from Mayer & Duschl (2005), for their fiducial Pop. III chemical composition. The Planck mean opacity for the dust is calculated in the same way as in Dopcke et al. (2011). Finally, the combined Planck mean opacity is the sum of gas and dust contributions, $\kappa_P \equiv \kappa_{gas} + \kappa_{dust}$.

By considering the maximum accretion luminosity for each case, we get that $\Gamma_{acc} = 4.9$, 0.9, 1.7, and $0.7 \times 10^3 (20\mathrm{AU/r})^2 \mathrm{erg\ s^{-1} g^{-1}}$, for $Z = 10^{-4}$, 10^{-5}, 10^{-6}, and 0 $Z_\odot$.

As these values are comparable to the other thermal processes at high densities (see Figure 3.3), it would seem that accretion luminosity heating

from the young protostars may have some effect on the way in the which the gas behaves. However without doing the radiative transfer explicitly, it is difficult to estimate how big this effect will be.

Although the amount of heating seems high, the dust cooling is a strong function of temperature in this regime, and so it could be that dust temperatures remain quite similar. One must also remember that the above estimates do not take into account the extinction and reprocessing of the radiation field that will occur in the optically thick region that surrounds the protostar. However even a factor of 2 change in the dust temperature will remove the dip in the $\rho - T$ phase diagrams that we show in Figure 3.2, and thus remove the ability of the dust to set a new length-scale for fragmentation.

3.5.3 Merging

Another effect that could change our results is the possibility of inelastic encounters between the protostars. Star formation in our simulation occurs at very high densities, where inelastic encounters between the new born protostars could occur. In similar conditions to the ones tested here, Smith et al. (2011, 2012) show that the estimated stellar radius could be as large as ~ 1 AU, a value comparable to the distances between the sink particles shown in Figure 3.6. By not accounting for merging of such objects, we could be overestimating the final number of fragments, although we expect new protostars to continue to form.

Since collisions may result in merging, we estimated this effect by comparing the sink particles distances and estimated radii. The stellar radii were calculated following Equation 3.5. By considering that every collision resulted in merging, we concluded that the number of merged objects is relatively the same for all simulations (see Table 3.2). Also when we compare the mode of star formation, the discrepancy on the mode of star formation for the $Z = 10^{-4} Z_{\odot}$ only becomes more evident. The particles that collided have most often masses higher than $0.1 M_{\odot}$, therefore the low-mass part of Figure 3.7 had not changed considerably. This means that the conclusions about the mode of star formation in Section 3.5 are not strongly affected by merging. The simulation with $Z = 10^{-4} Z_{\odot}$ remains with a more present-day-like stellar mass distribution, even when merging is considered.

Also in Figure 3.9 we show the fragmentation time, when merging is considered. The important fact that the fragmentation time is shorter than accretion timescale for $Z = 10^{-4} Z_{\odot}$ is not affected by merging. The noticeable change is that the ratio τ_{frag}/τ_{acc} becomes shorter for the simulation with $Z = 0$. This means that for this case, the overall fragmentation is

$Z/Z_\odot$	N_{am}	N_{merged}	Mean ($M_\odot$/yr)	Coll. Mean ($M_\odot$/yr)
0	14	5	0.34	0.65
10^{-6}	11	5	0.43	0.81
10^{-5}	12	7	0.39	0.53
10^{-4}	38	7	0.13	0.38

Table 3.2: Sink particle properties considering that all collisions resulted on merging. "N_{am}" is the remaining number of sink particles after merging, "N_{merged} is the number of those that could have merged. Note that N_{am} + N_{merged} recovers the number of sink particles (N) in Table 3.1. "Mean" refers to the new mean sink particle mass, and "Coll. Mean" refers to the mean mass of the particles that collided.

inhibited, and more high-mass objects will form.

3.6 Which physical mechanisms could be ignored?

Our aim with these calculations is to study the importance of dust cooling for fragmentation in high-redshift halos. To better understand star formation in this environment, additional physical processes should be considered as well.

Particularly, the low number of sink particles (≈ 20) and the small SFE (0.5%) do not permit to constrain the stellar IMF adequately. By running the calculations until the SFE goes towards higher values, uncertainties involving the fragments that formed during the simulations can be diminished. However, this does not appear to be computationally feasible with our current approach.

Sufficiently far enough away from the strongest sources, the effect will obviously drop to the point at which the physics in our current calculations are applicable. However if we look to Figure 3.6, we see that most of the fragmentation that we report is confined to a few tens of AU around the central protostar, and as such, the effects of the accretion luminosity are likely to change the picture that we present in this paper to some extent. We hope to explore this effect in a future study.

Another aspect of our model that could be improved upon are the dust opacities. The thermal evolution can be calculated more accurately if we use dust opacities that better represent the values expected for very low

metallicity environments. The dust opacity in our simulations correspond to values calculated for the Milky Way and then scaled with metallicity. This means that the opacity values for the $Z = 10^{-4}Z_{\odot}$ case are 10^{-4} times the dust opacity in the Milky Way. This approximation is probably not fully correct, and the use of a more accurate model (e.g. Todini & Ferrara 2001; Bianchi & Schneider 2007; Schneider et al. 2012; Nozawa et al. 2003, 2006) can change the value of the cooling in the region where fragmentation occurs. This change affects the local Jeans mass, and consequently the star formation behavior.

Furthermore, the available models give the dust composition for different scenarios in the early Universe, e.g. different supernovae progenitor masses (Schneider et al. 2012), and the use of such models would add another variable to the problem - the stellar population for the supernovae progenitors. One reasonable approach is to test different scenarios and see how they would affect the properties of the cluster of stars that forms. In this sense, the dust composition is a problem in itself that should be addressed. Since cooling affects the fragmentation behavior and mass accretion, a more realistic dust model improves the accuracy with which we can model star formation at low metallicities. We intend to address this issue in a future paper.

Finally, the inclusion of magnetic fields in the calculations could alter the fragmentation picture as it is presented in this study. They can be amplified during gravitational collapse (Schleicher et al. 2010a), generating values strong enough to delay the collapse (Schleicher et al. 2009; Sur et al. 2010; Federrath et al. 2011b,a; Turk et al. 2012). Analytic amplification values are calculated by Schober et al. (2012). From modeling present-day star formation, we know that the presence of magnetic fields can decrease the level of fragmentation, but cannot prevent it, for the expected saturation levels of a few percent (Peters et al. 2011; Hennebelle et al. 2011).

Chapter 4

A novel model for the stellar IMF

Since the seminal work by Salpeter (Salpeter 1955), raising the hypothesis of an initial mass function (IMF) enables astrophysicists to make enormous advances in their research. The first conclusion was that the total mass of the present stars is of the same order of magnitude as the total mass which was once in the form of main-sequence stars. In other words, it enabled Salpeter to infer the matter cycle in the ISM, and the role of the last stages of stellar evolution. Also, with a law for the stellar mass distribution of stars one can determine properties for the entire galaxy. Moreover, the IMF provides hints on the chemical content of stellar clusters and galaxies, and the link between the light from stars and the baryonic mass.

Observations have shown that the IMF is relatively constant over extreme changes in the environment. Even for environments with variation in density, pressure, metallicity by orders of magnitude, the median stellar mass remains somehow constant (Bastian et al. 2010).

By assuming it to be time-independent, Miller & Scalo (1979) were able to infer the IMF from the present-day mass function (PDMF). This was constructed from the luminosity function, and involved several assumptions (e.g. mass-luminosity relation, the distribution of stars perpendicular to the galactic plane, non-main-sequence correction, and main-sequence brightening correction). In this work, they extended the stellar mass distribution to an wider range of masses, where it could be fitted with a half log-normal function (in the low-mass part) plus a power-law (for the high-mass range).

With the model by Zinnecker (1984), it was possible to explain the log-normal shape in the low-mass range. The physical description for building up such a distribution required a hierarchical fragmentation, based on successive

stages. After each stage, the fragment would have a fraction of the total mass. Mathematically, each star has a mass corresponding to a successive multiplication of the cloud mass:

$$M_* = M_{cl} \prod_{i=1}^{n} (f_i/2), \tag{4.1}$$

where M_* is the final stellar mass, M_{cl} is the initial cloud mass, f_i denotes the mass conversion factor, and n is the number of steps in the hierarchy. For a cloud with $M_{cl} = 10^4 M_\odot$, the number of steps is approximately 5 (Bodenheimer 1978), this value is fixed for simplicity.

Then, such relation is divided in both sides by the average stellar mass:

$$\langle M_* \rangle = M_{cl} \prod_{i=1}^{5} (\langle f_i \rangle /2), \tag{4.2}$$

and the stellar mass in terms of the average stellar mass becomes:

$$\frac{M_*}{\langle M_* \rangle} = \prod_{i=1}^{5} \frac{f_i}{\langle f_i \rangle}. \tag{4.3}$$

By taking the logarithm of both stellar mass and product operator, the last becomes a summation:

$$\ln \frac{M_*}{\langle M_* \rangle} = \sum_{i=1}^{5} \frac{f_i}{\langle f_i \rangle}. \tag{4.4}$$

Finally, by applying the Central Limit Theorem (Cramér 1946), the distribution is a Gaussian in log-mass.

$$\xi \left[\ln \frac{M_*}{\langle M* \rangle} \right] \propto \exp \left[\frac{\ln^2 (M_* / \langle M* \rangle)}{2\sigma^2} \right], \tag{4.5}$$

with

$$\sigma = \frac{1}{N} \sum_{j=1}^{N} \sum_{i=1}^{5} \ln^2 \frac{f_i^j}{\langle f_i \rangle}, \tag{4.6}$$

where N is the total number of stars, and j refers to a particular star.

The model above accounts just for the low-mass part of the IMF. For the high-mass part, Bonnell et al. (2001a) investigated whether accretion in clusters could result in a power-law spectrum of stellar masses. They assumed that the mass accretion rate for each star ($\dot{M}_*$) depends on the

local gas density (ρ), its velocity relative to the gas ($V_{\rm rel}$) and the square of the accretion radius ($R_{\rm acc}$):

$$\dot{M}_* = \pi \rho V_{\rm rel} R_{\rm acc}^2. \tag{4.7}$$

There are two regimes inside the cluster which dominate the gravitational potential. When the gas component dominates, the accretion radius is given by the tidal-lobe radius ($R_{\rm tidal}$),

$$R_{\rm tidal} \approx 0.5 \left(\frac{M_*}{M_{\rm enc}} \right)^{1/3} R, \tag{4.8}$$

where M_* is the stellar mass, and $M_{\rm enc}$ is the enclosed mass in the stellar position R in the cluster.

When stars dominate the potential, the accretion radius is better described by the Bondi-Hoyle formalism (Bondi & Hoyle 1944):

$$R_{\rm BH} = \frac{2GM_*}{V_{\rm rel}^2 + c_s^2}, \tag{4.9}$$

where $R_{\rm BH}$ is the Bondi-Hoyle accretion radius, M_* is the stellar mass, $V_{\rm rel}$ refers to the relative velocity between the gas and the star, and c_s is the local sound speed.

This leads to clusters with a slope for the mass spectrum (γ) for the low-mass stars, and a steeper value for the high mass stars:

$$dN \propto M_*^{\gamma} dM_* \begin{cases} \gamma = -1.5 & \text{if } M_* \lesssim 0.5 M_\odot \\ -2.5 > \gamma > -2.0 & \text{otherwise,} \end{cases} \tag{4.10}$$

where N is the number of stars, and the Salpeter value for γ is -2.35. Although the competitive accretion picture is consistent with mass segregated clusters, it needs to assume an initial segregation in order to develop a $\gamma \leq -2$.

In Section 3.5 we showed that the characteristic time for fragmentation and accretion vary with metallicity. This will most certainly have effects on the stellar IMF: does a faster fragmentation affect the slope on the IMF high mass range? Does it change the characteristic fragment mass? How similar to the canonical IMF would be the cluster described in the previous chapter?

With the aim to answer such question, we developed a model that took into account fragmentation and accretion. The share of the accreted mass between the stars was done based on the competitive accretion picture, however the assumptions here were simpler. We did not assume any initial cluster, nor mass segregation. The assumptions were just that a gas cloud fragments,

and the new formed objects accrete mass. In this was, the *ad hoc* hypothesis inconvenience was transferred to the free parameters in the model.

Hereafter, we will present a theoretical background, and also describe how the model works. The aim is to examine how the IMF develops in a cluster that is still growing, and understanding the parameters described in the next sections will help on this task.

4.1 A simple view of the IMF

In this chapter we address such problem, with the goal of constructing a consistent model of the IMF. Hereafter we will describe how the model works, and how its parameters are related to physical quantities.

4.1.1 Jeans instability

In order to build a model for the distribution of stellar masses, one has to consider what is the characteristic mass for the fragments. If one considers an isothermal homogenous sphere, both the sound crossing time and the free-fall time can be calculated.

$$t_{\rm sound} = \frac{R}{c_s} \tag{4.11}$$

$$t_{\rm ff} = \frac{1}{\sqrt{G\rho}}, \tag{4.12}$$

where $t_{\rm sound}$ is the sound crossing time, $t_{\rm ff}$ is the free-fall time, R is the radius of the sphere, c_s is the local sound speed, and ρ refers to the gas density.

By making both to be equal, the time for the gas to respond to the contraction, which would represent an increase in temperature, is the same as the time for contraction. Instability occurs when the time for collapse is shorter than the sound speed. With that, one can derive characteristic length-scales (λ_J) and masses (M_J) for the fragments:

$$\lambda_J = \frac{c_s}{\sqrt{G\rho}} \tag{4.13}$$

$$M_J = \frac{\pi}{6}\frac{c_s^3}{G^{3/2}\rho^{1/2}} \tag{4.14}$$

In reality, the situation is often more complicated. Normally the gas is not isothermal during the collapse, nor is thermal energy the only energy that

acts to prevent the collapse. For simplicity, we ignore here effects that change the Jeans instability picture. Moreover, when the gas reaches the optically thick regime (see Figure 2.1), radiation cannot scape. The further evolution of the gas is adiabatic, and in this regime, fragmentation is unlikely. Thus, by assuming that the characteristic mass of the collapsing fragments is a good approximation for the stellar value, M_J represents for the characteristic mass of the stars.

4.1.2 Mass accretion

In the competitive accretion picture (Bonnell et al. 2001b), the mode of accretion plays a crucial role in determining the final stellar mass distribution. For gas-dominated potentials, the accretion radius is given by the tidal-lobe radius (Bonnell et al. 2001b), since the gravitational potential from de star dominates gas inside the tidal lobe. This leads to a stellar mass accretion rate ($\dot{M}_*$) proportional to the stellar mass to the power 2/3:

$$\dot{M}_* \propto M_*^{2/3}. \tag{4.15}$$

Finally, the mass spectrum has the form $dN \propto M_*^{-3/a} dM_*$, where a depends on the gas density profile in the form $\rho \propto R^{-a}$. For stellar-dominated potentials, however the accretion radius is given by the Bondi-Hoyle radius. Once the gravitational potential from stars is dominant, the stars virialize and their velocities become large. At this point, $R_{\rm BH}$ becomes small when compared to $R_{\rm tidal}$, and it is a better description of the accretion radius Bonnell et al. (2001a). In this regime, the mass accretion rate is proportional to the stellar mass to the power 2:

$$\dot{M}_* \propto M_*^2. \tag{4.16}$$

This leads to a mass spectrum of the form $dN \propto M_*^{-\gamma} dM_*$, with γ between -2 and -2.5. This shows that the mode of accretion by the stars plays an important role in determining the mass spectrum. Moreover, the general formula for mass accretion can be rewritten as $\dot{M}_* \propto M_*^{\alpha}$. This formalism will be important to build up the model presented here.

Overall, the competitive accretion picture helps to understand how the IMF is built up. The problems, however are that it requires an initial mass segregation to develop a slope $\gamma < -2$ and that the low-mass range ($M_* < 0.3 M_\odot$) is described just by a power-law of a single slope, while observational studies show that this is not the case (see e.g. Chabrier 2003; Kroupa 2002).

4.1.3 Fragmentation rates

The mode of fragmentation for gas clouds has been investigated in many studies (e.g. Hoyle 1953; Ferrini et al. 1990; Stamatellos & Whitworth 2009; Smith et al. 2009b; Clark et al. 2011a,b). Also, understanding the interplay of fragmentation and accretion rates has shown to be essential in order to model non-standard IMFs (Dopcke et al. 2012). The physical mechanism behind variations in the fragmentation rates resides on the Jeans mass at the point where the gas becomes optically thick ($\tau > 1$), and no further fragmentation is expected (Rees 1976; Silk 1977). Since the Jeans mass depends on temperature and density,

$$\dot{M}_J \propto \rho^{-1/2} T^{3/2}, \tag{4.17}$$

it is important to have a self-consistent description of the thermal evolution of the gas during the collapse. Furthermore, the ability of the gas to cool depends on its chemical composition, thus with a model that includes the most important chemical reactions, one can predict the level of fragmentation of the gas.

4.1.4 Characteristic masses

Closely related to the fragmentation rate is the initial mass of the fragments. By having a lower initial mass for the fragments, the fragmentation rate can be enhanced when the mass of infalling gas is kept constant. In Jappsen et al. (2005), the authors showed that the peak in the mass spectrum was related to the position of an inflection point in the effective polytropic exponent ($\gamma_{\rm eff}$ - not to be mistaken with the γ for the slope in the IMF). They found that the density at which $\gamma_{\rm eff}$ changes from below unity to above unity selects a characteristic mass scale.

Spherical collapse can occur for values of $\gamma_{\rm eff} < 4/3$, but this kind of collapse is not likely to lead to fragmentation, and the collapsing parts of the gas tend to fall into the center of the gravitational potential well. High fragmentation is more likely when many centers of collapse are formed, and this is enhanced in thin filaments. In order to form thin filaments $\gamma_{\rm eff} < 1$ is required (Larson 2005). It was also show by Peters et al. (2012) that for $\gamma_{\rm eff} < 1$, the formation of central virialized cores is suppressed. Also, the flow develops strong shocks, which create extended filaments, thus increasing fragmentation.

This way of thinking tells us that once the equation of state (EOS) for the gas is determined, the most likely value for the stellar mass is also defined. The remaining questions would be then just regarding the shape of the IMF.

4.2 Model

In this section we discuss the main ingredients for the model. Our analysis will rely on four main quantities: initial stellar mass (M_i), total cluster mass accretion ($\dot{M}$), fragmentation rate ($\dot{n}$), and the accretion power α, for $\dot{M}_* \propto M_*^\alpha$. Note that M refers to the total cluster mass, while M_* refers to an individual star. With these four properties, we can model the stellar mass distribution in time. In this section, we describe the algorithm for building the IMF.

A new-born object (o1) has an initial mass M_i. After a time

$$t_{\rm frag} \equiv \frac{1}{\dot{n}}, \tag{4.18}$$

a new fragment is formed (o2). Note that the time-step in this model is simply $t_{\rm frag}$. At this point the mass accreted by o1 is related to $\dot{M}$ by

$$M_{acc,1} = \frac{\dot{M}}{\dot{n}} - M_i, \tag{4.19}$$

where $M_{acc,1}$ is the mass accreted by o1. In this way, the mass accreted by the cluster is

$$\Delta M = \dot{M} t_{\rm frag} = \frac{\dot{M}}{\dot{n}} = M_{acc,1} + M_i. \tag{4.20}$$

When the third object is formed (o3), it is necessary to share the total accreted mass between the previous objects. To do this, we make use of the α parameter. The accretion by a general object oi ($M_{acc,i}$) is defined as

$$M_{acc,i} = \left(\frac{\dot{M}}{\dot{n}} - M_i \right) \frac{M_i^\alpha}{\sum_{j=1}^{n} M_j^\alpha}. \tag{4.21}$$

where n is the number o stars in the cluster.

4.2.1 Building up a stellar cluster

Suppose that we have a cluster with N stars, with masses M_1, M_2, ..., M_N. At time $t = 0$, we have:

$$M_1 = M_2 = ... = M_N = 0$$

After the clock starts to run, the stars start to form. Here, time is in units of fragmentation time ($t_{\rm frag}$), thus at $t = 0$, there is no fragment, at $t = 1$

there is one fragment, and so on. In this simple model, we assume that the fragmentation time remains constant as the cluster builds up. At time $t = 1$, we therefore have

$$\begin{aligned} M_1 &= M_i \\ M_2 = ... = M_N &= 0, \end{aligned}$$

where M_i is the initial mass for all the stars, while at $t = 2$ we have

$$\begin{aligned} M_2 &= M_i \\ M_1 &= M_1 + M_{acc} \\ M_{acc} &= \dot{M}\Delta t - M_i \\ M_1 &= M_1 + \dot{M}\Delta t - M_i \\ M_3 = ... = M_N &= 0 \end{aligned}$$

Note that in order to make the total mass increase equal to $\dot{M}\Delta t$, the accretion by M_1 has to be subtracted by M_i, which is the initial mass for M_2. Also, $M_1 = M_1 + M_{acc}$ indicates that M_1 is accreting M_{acc}.

At time $t = 3$, we have

$$\begin{aligned} M_3 &= M_i \\ M_4 = ... = M_N &= 0 \\ M_{acc} &= \dot{M}\Delta t - M_i \\ M_2 &= M_2 + ? \\ M_1 &= M_1 + ? \end{aligned}$$

At this point, we have pre-existing stars, and we need to make a decision about how they are going to accrete. One possibility is that they accrete equal amounts of mass:

$$\begin{aligned} M_1 &= M_1 + M_{acc}/2 \\ M_2 &= M_2 + M_{acc}/2 \end{aligned}$$

Another possibility is that they accrete proportionally to their masses:

$$M_1 = M_1 + \frac{M_{acc} M_1}{M_1 + M_2}$$
$$M_2 = M_2 + \frac{M_{acc} M_2}{M_1 + M_2}$$

In our model, accretion is slightly more general then this. We assume that they accrete proportionally to their masses to the power α.

$$M_1 = M_1 + \frac{M_{acc} M_1^\alpha}{M_1^\alpha + M_2^\alpha}$$
$$M_2 = M_2 + \frac{M_{acc} M_2^\alpha}{M_1^\alpha + M_2^\alpha}$$

Now we can generalize for a given star k at the time $t = j$. The masses for the stars depends on their previous state at $t = j - 1$. Thus for a star k with mass $M_{k,t=j-1}$ at $t = j - 1$, the new mass of the star $M_{k,t=j}$ at time $t = j$:

$$M_{k,t=j} = \begin{cases} M_{k,t=j-1} + M_{acc,k} & \text{for } k < j \\ M_i & \text{for } k = j \\ 0 & \text{for } k > j \end{cases} \tag{4.22}$$

$$M_{acc,k} = \frac{M_{acc}(M_{k,t=j-1})^\alpha}{\sum_{q=1}^{j-1}(M_{q,t=j-1})^\alpha} \tag{4.23}$$

$$M_{acc} = \dot{M}\Delta t - M_i \tag{4.24}$$

Note that the summation in Equation 4.23 takes into account all the stars with masses higher than zero at $t = j - 1$. Also, when $\alpha = 0$, the stars accrete equal amounts of mass, while for $\alpha = 1$, they accrete proportionally to their masses.

4.3 Comparison with previous models

In this section, we defend why this model improves upon previous descriptions for the IMF. The search for the leading mechanisms that shape the IMF has been the goal of many previous studies (e.g. Bonnell et al. 2001b; Hennebelle & Chabrier 2008; Krumholz 2011). Typically, these works invoke dominant physical processes, that determines the shape of the IMF.

For Bonnell et al. (2001b), the dominant process is the mode of accretion by the stars. They use an adapted tidal-lobe accretion which includes the

effect of companion stars. Such process leads to two power-laws for the stellar mass distribution, with slopes described in Equation 4.10.

Invoking a different process, but using a similar sequence of thoughts, the Hennebelle & Chabrier (2008) model assumes that the first structures in the cluster are built due to supersonic turbulence. This will lead to the formation of structures following a Press-Schechter theory of structure formation (Press & Schechter 1974). Thermal and non-thermal processes lead finally to a logarithmic dependance of the masses. All things considered, the final shape of the IMF is log-normal, with the power-low for high masses dependent on the Mach number.

The Krumholz (2011) model describes the characteristic mass of stars from fundamental constants, with small contribution from environmental conditions. It relies on the process of radiative feedback from stars, which regulates the fragmentation of the gas.

The overall trend of such models is the attempt to explain the stellar IMF by relying on no more than a couple of physical processes. This method is tempting because it reduces the complexity of the problem. However, when there are many theories that can explain the same observable, which one do you choose? The uncertainties related to the observables are large enough that it makes it hard to exclude any of the models.

The special feature of the model described here is that it does not assume any main physical driving mechanism to shape the IMF. Accretion is described in a mathematical fashion with two limits, one where all fragments accrete evenly, and the other where the most massive accrete at a higher rate. This is done by using a free parameter (α) which can be modified in accordance to the physics of the problem. The other main free parameter is the average stellar mass ($\langle M_* \rangle$), which is also dependent on the physics of the model. This model is more adequate to an expected variability of the IMF with the environmental conditions.

In particular, in order to explain the results of hydrodynamical models for star formation in the early Universe, which typically produce a higher characteristic mass (e.g. Hosokawa et al. 2011; Clark et al. 2011a; Greif et al. 2011b), a model that accommodate such variability is more robust. In addition to that, observational data require a top-heavy IMF to explain the characteristics of some Galactic globular clusters (Marks et al. 2012; Kroupa et al. 2011), and also the high fraction of extremely metal-poor stars that are C-rich (Suda et al. 2012). Thus making necessary for the models to describe not just the formation of the present day IMF, but also other shapes that it might develop.

Nevertheless, models should not only explain simulations and observations, but should also have predictive power.

The model presented in this work aims to explain simulations and observations, and can also constrain cluster formation parameters, such as age, number of stars, and the total cluster mass. The model is also able to make predictions on the future of star forming regions, and speculate on the IMF for different modes of star formation. In the next sections we present examples of that.

4.4 Comparison with simulations

One possible application for this model is to simplify the analysis of simulations. In simulations, many time dependent physical parameters are treated. In this model, there are just five free parameters ($\dot{M}$, $\dot{n}$, M_i, α, and time), which will later be reduced to three ($\langle M \rangle$, α, and time, see Section 4.5).

Likewise, the outcome of simulations for star formation can produce such values. Sink particles are widely used, and they have all properties that could be translated to mass, mass accretion, initial mass, etc. This means that numerical studies could use this model as a tool to simplify their analysis. The simulations in Dopcke et al. (2012) are described in Chapter 4. In Girichidis et al. (2012), they test the influence of initial conditions for star formation. More specifically, how star formation is affected by different: density profile, mode of turbulence, and random seeds for the turbulence. The advantage of using their results is the fact that the number of sink particles is typically more than five times the one we achieved in Dopcke et al. (2012). Thus, the statistical properties for the calculated parameters are better stablished. We sill now apply our model to simulations from Dopcke et al. (2012) and Girichidis et al. (2012).

4.4.1 Simulations of star formation at low metallicity

We used the results of the simulations of low metallicity star formation presented in Dopcke et al. (2012) and in Chapter 4 to derive values for α, $\dot{n}$, $\dot{M}$ and M_i as follows:

α – Alpha is the slope for the linear regression of equation:

$$\log \dot{M} = \beta + \alpha \log M \tag{4.25}$$

where M and $\dot{M}$ refer to the sink particle mass and mass accretion, respectively, at a given snapshot.

Each snapshot thus gives a value for the slope α and the intercept β. The regression was calculated for each snapshot (≈ 1/year).

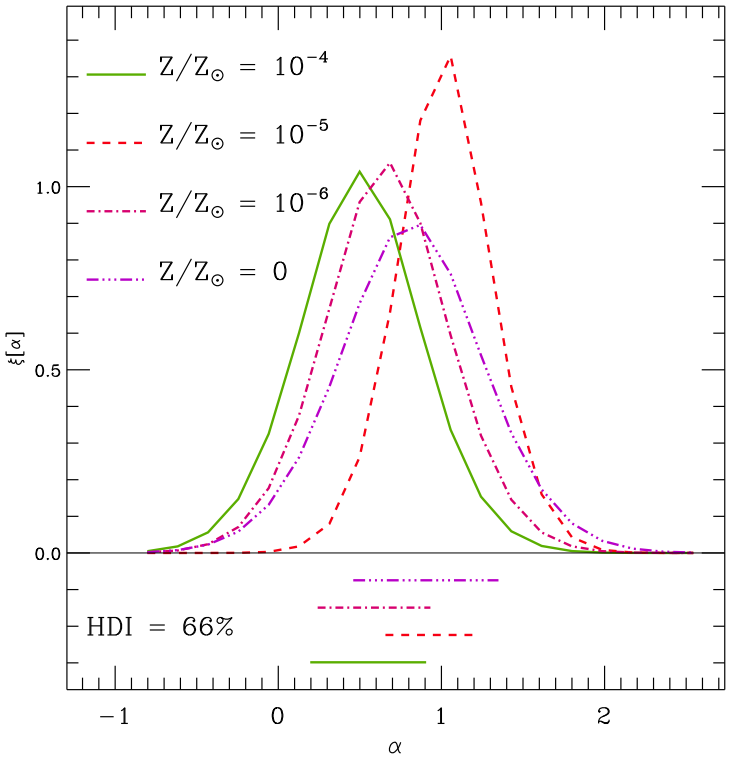

Figure 4.1: Gaussian fit for α and its 66% highest probability density interval (HDI), for $Z = 10^{-4}$, 10^{-5}, $10^{-6} Z_{\odot}$, and zero. The values presented here are based on the simulations in Dopcke et al. (2012)

The values for α fluctuate over time, and in order to apply the model to the simulations, we will use the most likely value, as well as values slightly below and above. With that, we can understand which are the values and their variations that affect most the IMF calculated with the model. The gaussian fits for the distribution of values of α for various metallicities is presented in Figure 4.1. There we show a 66% highest probability density interval (HDI). The extremes of this interval and the most likely value will be used later to calculate modeled IMFs and compared these with the IMF from the simulations (see Figure 4.9).

$\dot{n}$ – $\dot{n}$ is the fragmentation rate, which is calculated by taking the number of fragments and dividing by the time since the first fragment formed. A gaussian fit for the distribution of values calculated in various snapshots is shown in Figure 4.2

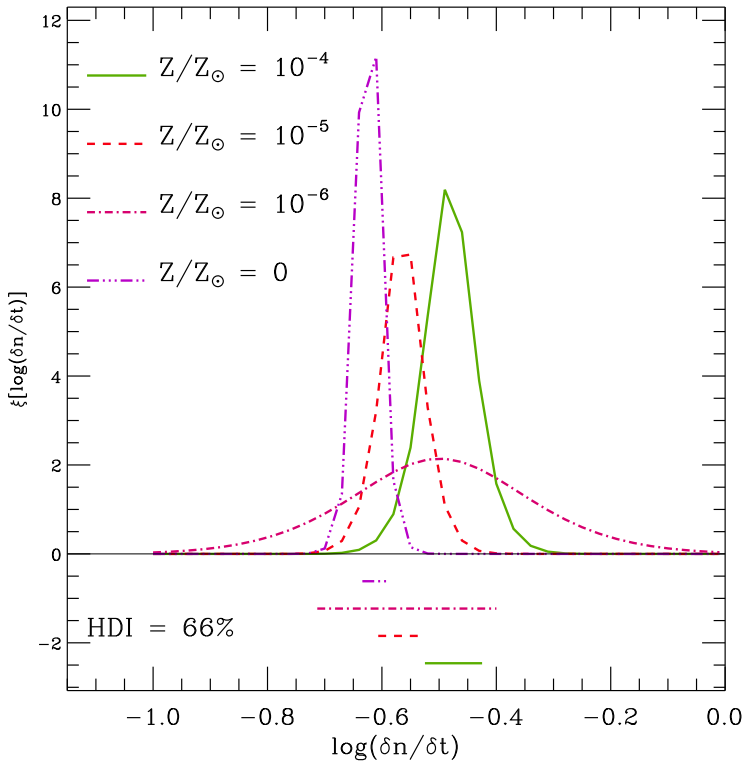

Figure 4.2: Gaussian fit for the fragmentations rate and its 66% highest probability density interval (HDI), for $Z = 10^{-4}$, 10^{-5}, $10^{-6} Z_{\odot}$, and zero. The values presented here are based on the simulations in Dopcke et al. (2012).

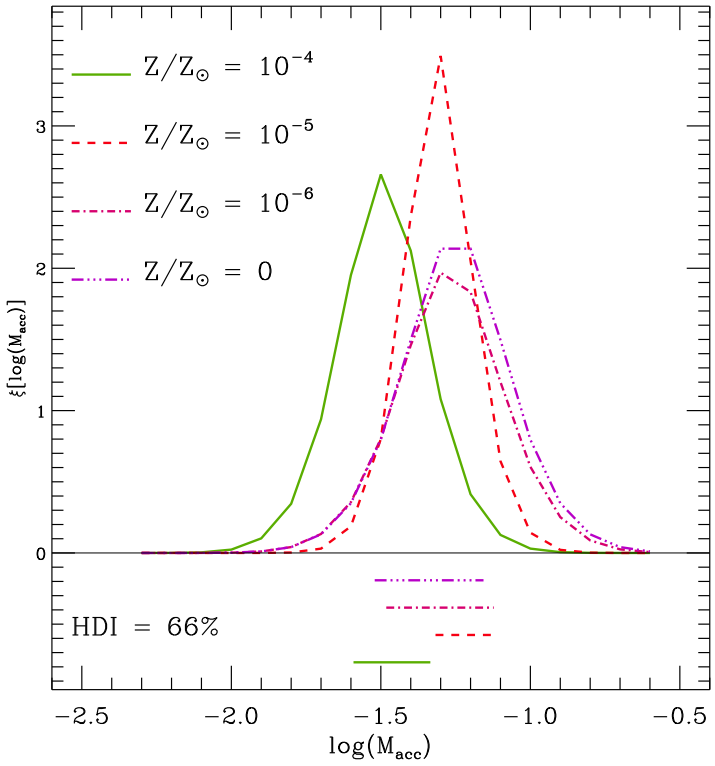

Figure 4.3: Gaussian fit for the mass accretion rate and its 66% highest probability density interval (HDI), for $Z = 10^{-4}$, 10^{-5}, $10^{-6} Z_{\odot}$, and zero. The values presented here are based on the simulations in Dopcke et al. (2012).

$\dot{M}$ – $\dot{M}$ is the mass accretion rate, which is calculated as the change in the total mass in sink particles divided by the time since the first fragment formed. This value was calculated for various snapshots, and fits for their distributions are shown in Figure 4.3.

M_i – M_i is the initial mass for the stars in the model and to obtain such value from the simulations, we use the initial sink particle mass. Note that this value is affected by resolution, since the minimum mass for the sink particles is 100 SPH particles, which is solar values gives $2.5 \times 10^{-3} M_{\odot}$. After forming, the sink particles accretes the gas around its Jeans radius, thus setting $M_i \approx M_J$ at the point in density where the sink particles form. That explains why M_i is lower for $Z = 10^{-4} Z_{\odot}$ than the value for the other metallicities (see Figure 4.4). For $Z = 10^{-4} Z_{\odot}$, the temperature (and thus M_J) is considerably lower at the point in density where the sink particles

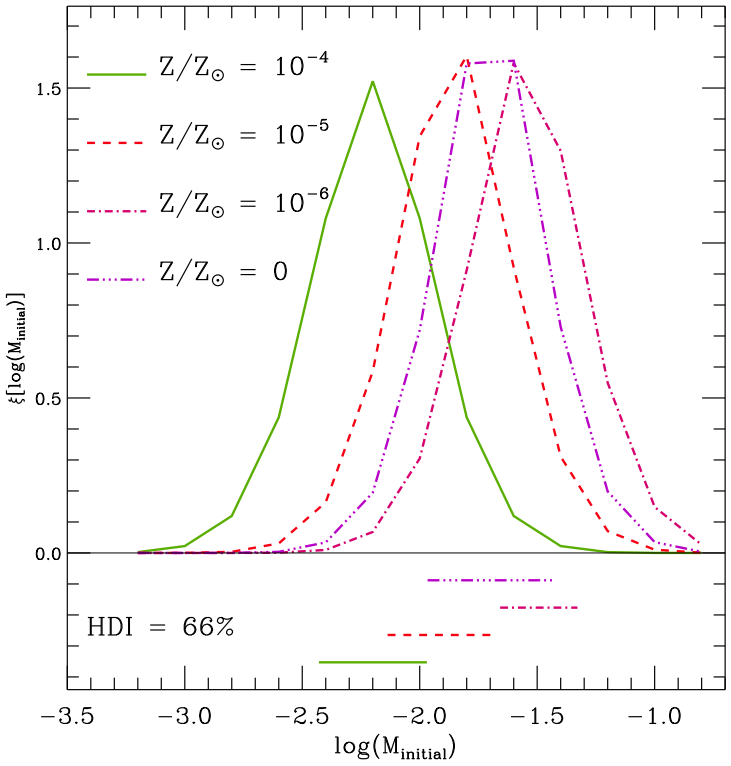

Figure 4.4: Gaussian fit for the initial sink mass and its 66% highest probability density interval (HDI), for $Z = 10^{-4}$, 10^{-5}, $10^{-6} Z_{\odot}$, and zero. The values presented here are based on the simulations in Dopcke et al. (2012).

form. Moreover, the sink particles do not accrete the gas in their Jeans radius instantaneously, and the value that we obtain for M_i will also depend on the point in time where it is calculated. Although M_i is considerably biased by these effects, variations in M_i have shown not to affect the high-mass part of the modeled IMF (see Figures 4.9 and 4.13).

4.4.2 Correlations

Here we present a graph showing the correlation between the various properties studied above (Figure 4.5).

It is important to notice here that there are correlations that simply result from the input data and the ones relevant to the model. The good correlation between time (t) and total mass (M) just indicates that over time the total mass in sink particles increases. A perfect correlation (full circle) would indicate constant mass accretion. More interesting, however,

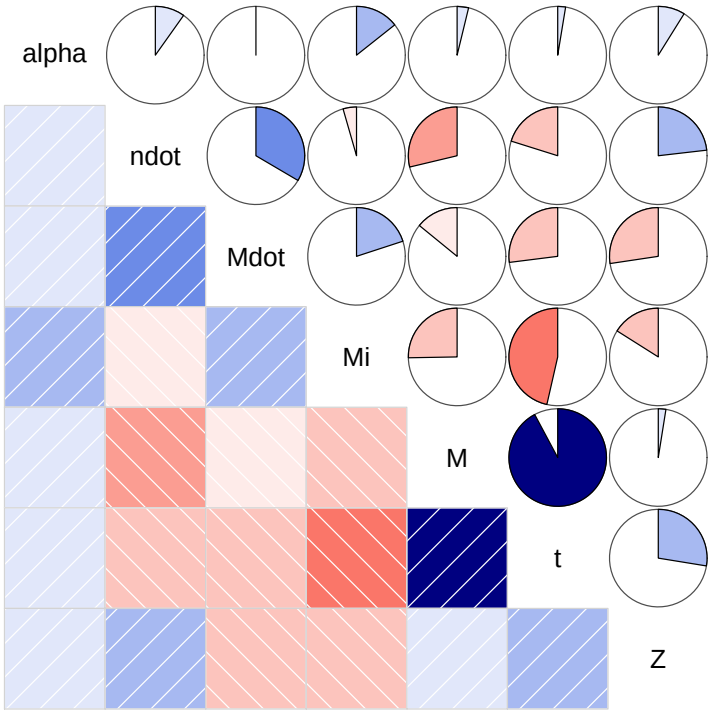

Figure 4.5: Correlations between the sink particles properties. Blue indicates correlation and red anti-correlation. The filling of the circles indicate the level of correlation, which is also emphasized the the darkness of the colors. The dark blue in the total mass (M) and time (t) indicates high correlation. The squares in the lower part of the plot also represent graphically those correlations. Positive correlations have stripes from bottom-left to top-right and are shown in blue, while negative correlations have stripes from top-left to bottom-right and are shown in red. The color scheme is the same for the stripes and the circles.

are the correlations that might indicate that some parameters in the model are correlated. A high degree of correlation between one or more parameters would allow the total number of parameters to be reduced, thus making the model simpler. A "perfect model" would have the lowest number of totally independent (incorrelated) parameters.

The first feature to notice is the lack of correlation between α and any other parameter. Second, the fragmentation rate has two noticeable correlated properties. The mass accretion rate responds naturally to the fragmentation, since every time fragmentation happens, the total mass in sink particles increases. The counterintuitive feature is that the total mass is anti-correlated with the fragmentation rates. As we have seen in Chapter 3, over time the central regions of our simulated systems become dominated by sink particles, leaving little gas available for fragmentation. Also, it is important to notice that the fragmentation rate increases with metallicity. This is the mechanism that explains the difference in the sink mass distribution favoring lower mass objects for higher metallicities (see also Chapter 3, Section 3.4).

Third, the mass accretion rate is anti-correlated with time, which means that it decreases over time. This means that inflow of gas mass towards the center of the potential well is not yet self-regulated. At the end of the simulations examined here, just 0.5% of the gas has been accreted onto sinks, and it is very unlikely that the accretion has ceased. Also the mass accretion rate is anti-correlated to the metallicity. For higher metallicities two phenomena are fundamental to shape the IMF, the higher fragmentation, and lower accretion.

Fourth, the initial mass is highly anti-correlated with time, which means that over time the initial mass decreases. This happens because there are objects in the central of the potential well that are accreting. This prevents fragmentation from occurring in the densest gas, meaning that most of the later fragmentation occurs in the accreting disk around the central cluster. Less gas is available here, and hence the masses of the new-born fragments are smaller. A weaker correlation is related to the total mass in sinks, which is another way to see the relation to time, since the total mass in sinks increases with time in the accreting cluster. Finally, the initial mass is smaller for higher metallicities, which shows that the Jeans mass is smaller for higher metallicities.

From this analysis, we see that $\dot{M}$ and $\dot{n}$ are not independent. We can therefore further improve the model in this case by merging both parameters in one. Namely, by dividing $\dot{M}$ by $\dot{n}$, we obtain the average mass $\langle M \rangle$, $\dot{M}/\dot{n} \equiv \langle M \rangle$. This is a good substitute, because it can also be obtained in both simulations and observations. Moreover, $\langle M \rangle$ can be related to the Jeans mass the the point of fragmentation. By reducing the number of free

parameters, it will be easier to understand the most important features of the model and the science it aims to reproduce (i.e. the IMF).

4.4.3 Analysis of simulations using this model

In order to get a better understanding of the simulations, we analyze them by running models for the IMF. The parameters for the model are acquired from the simulations, where we use the most frequent value and the borders of the 66% HDI (see Section 4.4). First, we set the total mass in the cluster to be the same as in the simulation. This will later be changed, however allowing us to predict what would happen if the cluster continue to evolve with the same parameters, but for a longer time.

By running the model with the parameters taken from the simulation, we can calculate a modeled IMF. This can be compared with the one from the simulation (see Figures 4.6 to 4.9). There, it can be seen that the model recovers qualitatively the mass distribution. Moreover, it is also possible to evaluate the effects of changing some parameters. For instance, varying M_i (lowest panel) only influences the MF for objects with $M < 10^{-2} M_\odot$, but leaves the majority of it unaltered. This is easy to understand, as most of the objects in the mass function have masses $M \gg M_i$.

The analysis of the simulated cluster using this model is an interesting test of the model, but due to the low number of objects ($n < 45$), further conclusions could not be derived. However, the adaptability of the model enables us to predict the future development of the cluster, by assuming that the key parameters remain constant. Here, we wuppose that the cluster reached $1000 M_\odot$. With this assumption, we are neglecting feedback effects from the assembling cluster on the infalling gas. The result of such model is shown in Figure 4.10.

The IMF that results from evolving the cluster in this fashion shows that the expected slope for the high-mass end of the IMF is very close to the Salpeter (1955) one. More interesting however, is that the slope for the higher metallicity is steeper than the others. Important to notice here is that the cut-off in mass might play an important role in the stellar distribution. Equally important is the average stellar mass, which is a parameter more essential to the distribution of masses than the slope for the high-mass part.

Furthermore, this model introduces a new capability, which is to compare individual mass accretion rates. The distribution of stars predicted by the model can be compared with the distribution measured in the simulations. We performed such a comparison and the result is shown in Figure 4.11.

From this comparison, we can learn a few things from the model. Since it uses a constant accretion rate, some differences between model and simu-

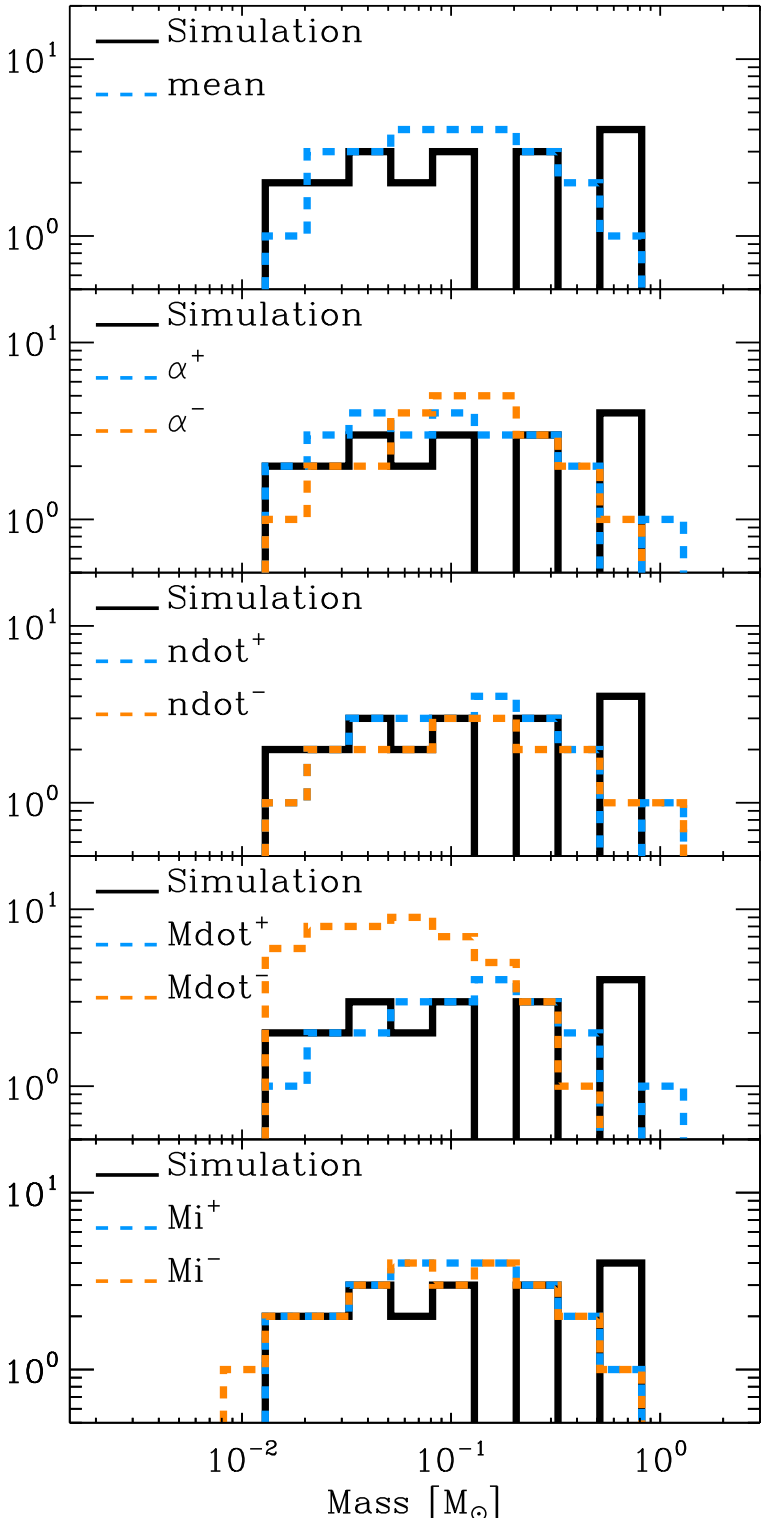

Figure 4.6: Comparison of the model IMF with that found in the $Z = 0$ simulation from Dopcke et al. (2012). The lines marked as "mean" refer to the model that used the mean value for the variables α, $\dot{n}$, $\dot{M}$, and M_i. The lines marked with $^+/^-$ refer to models that used the mean values of the other variable, but for that specific variable, the value used was the upper/lower value of the 66% HDI (see Section 4.4).

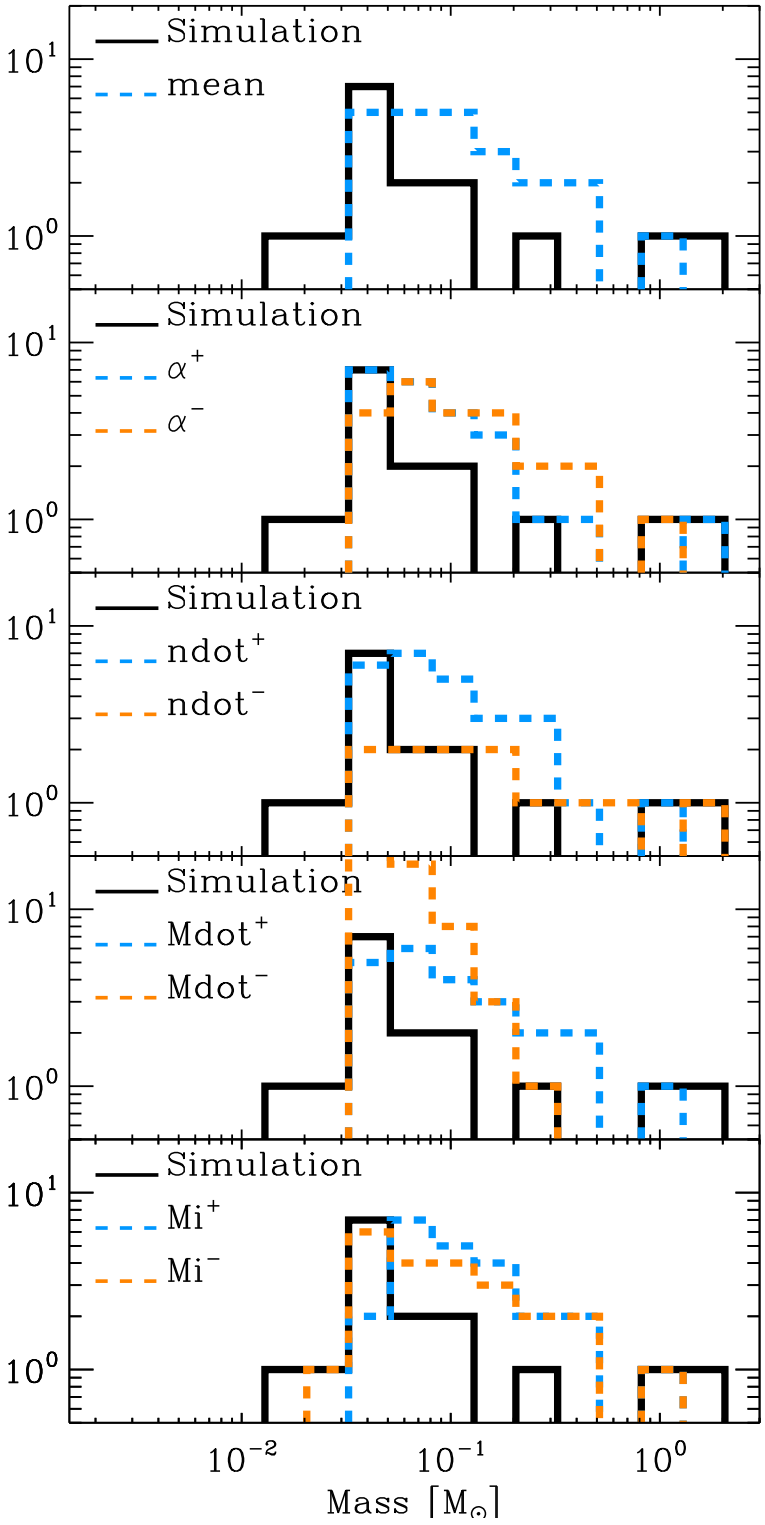

Figure 4.7: Same as figure 4.6, but for $Z = 10^{-6} Z_{\odot}$.

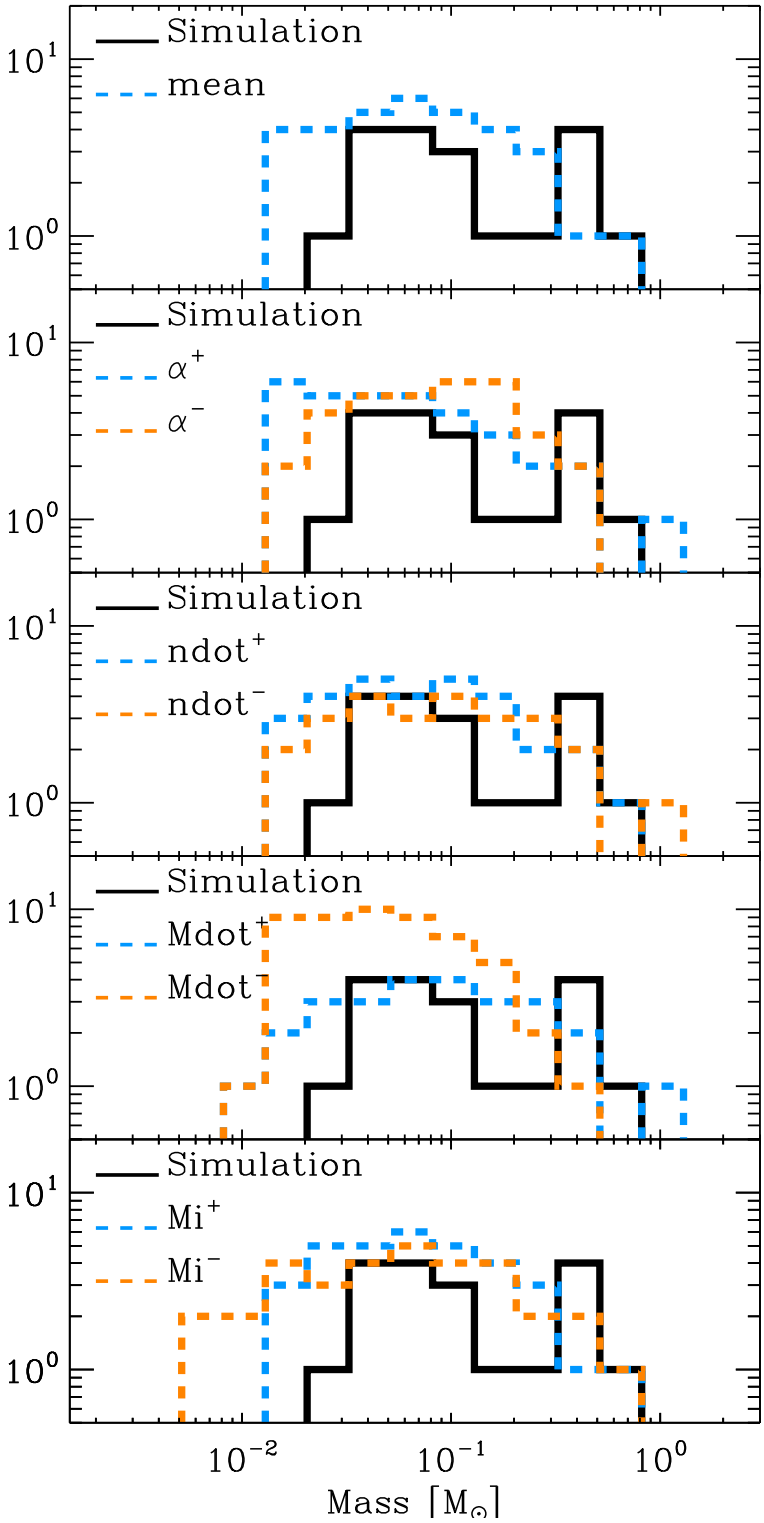

Figure 4.8: Same as figure 4.6, but for $Z = 10^{-5} Z_{\odot}$.

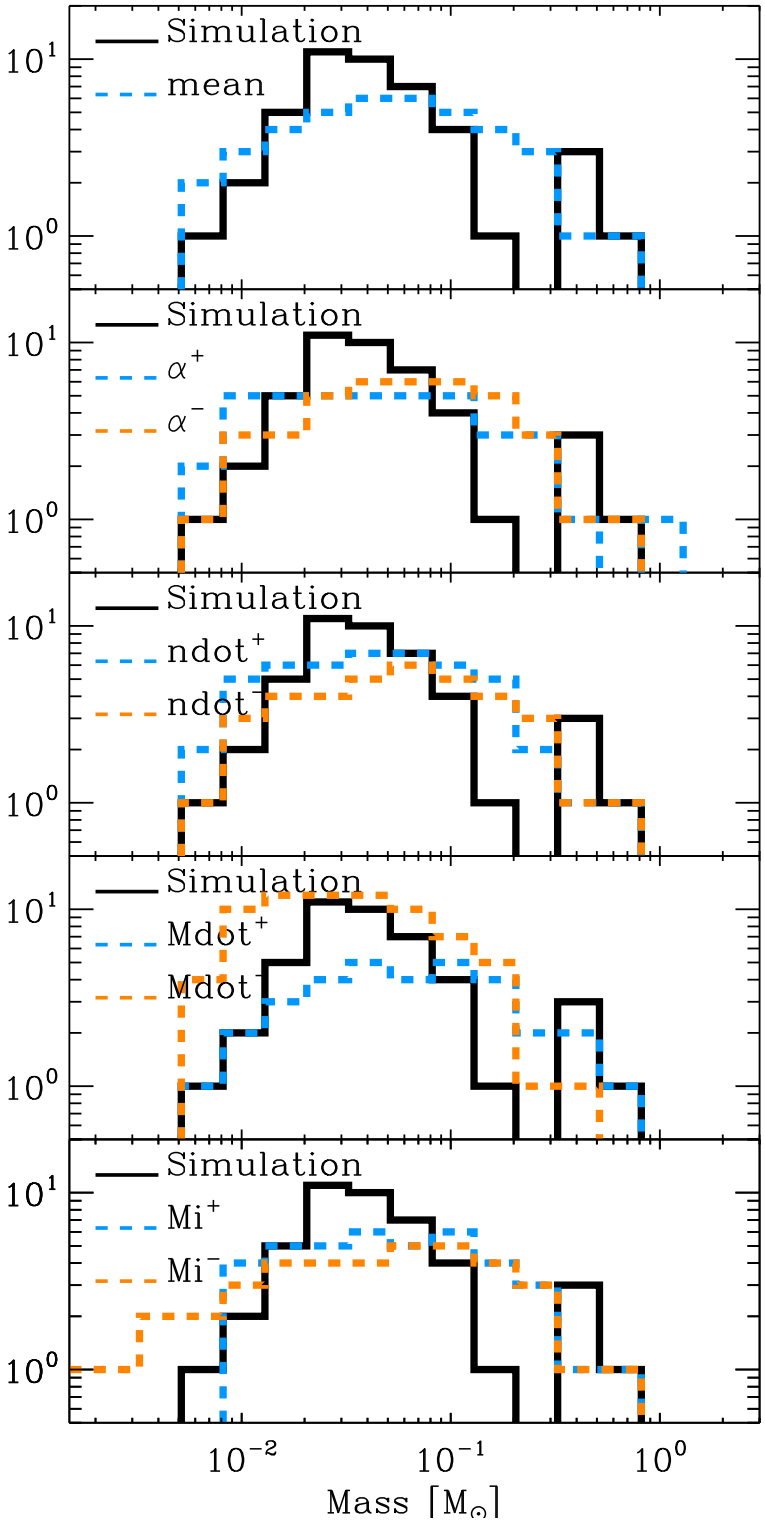

Figure 4.9: Same as figure 4.6, but for $Z = 10^{-4} Z_{\odot}$.

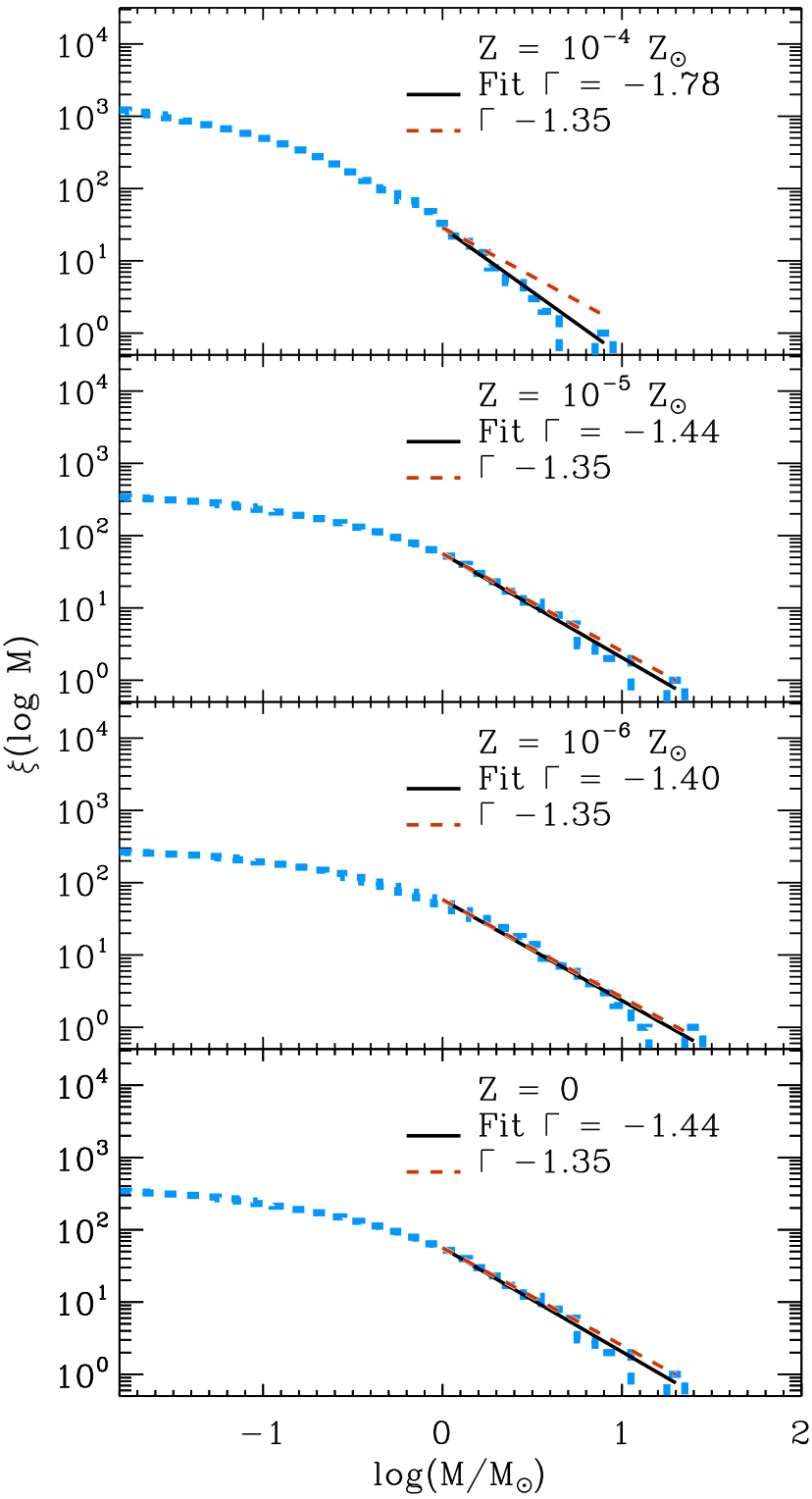

Figure 4.10: Predicted IMF at the point where the total cluster mass is 1000 $M_\odot$. The parameters for the models are $\alpha = 0.7$ and $M_i = 0.01 M_\odot$. For $\dot{n}$ and $\dot{M}$, we used the average values from simulations. Note that by assuming that the parameters do not vary from their initial values, we are assuming that stellar feedback does not have a strong effect on the cluster assembly. We opted for a constant value for α to make the comparison easier. This can be justified from the wide variance in α (see Figure 4.1. Also, the parameter M_i was set constant because the shape of the IMF showed to be insensitive to this parameter.

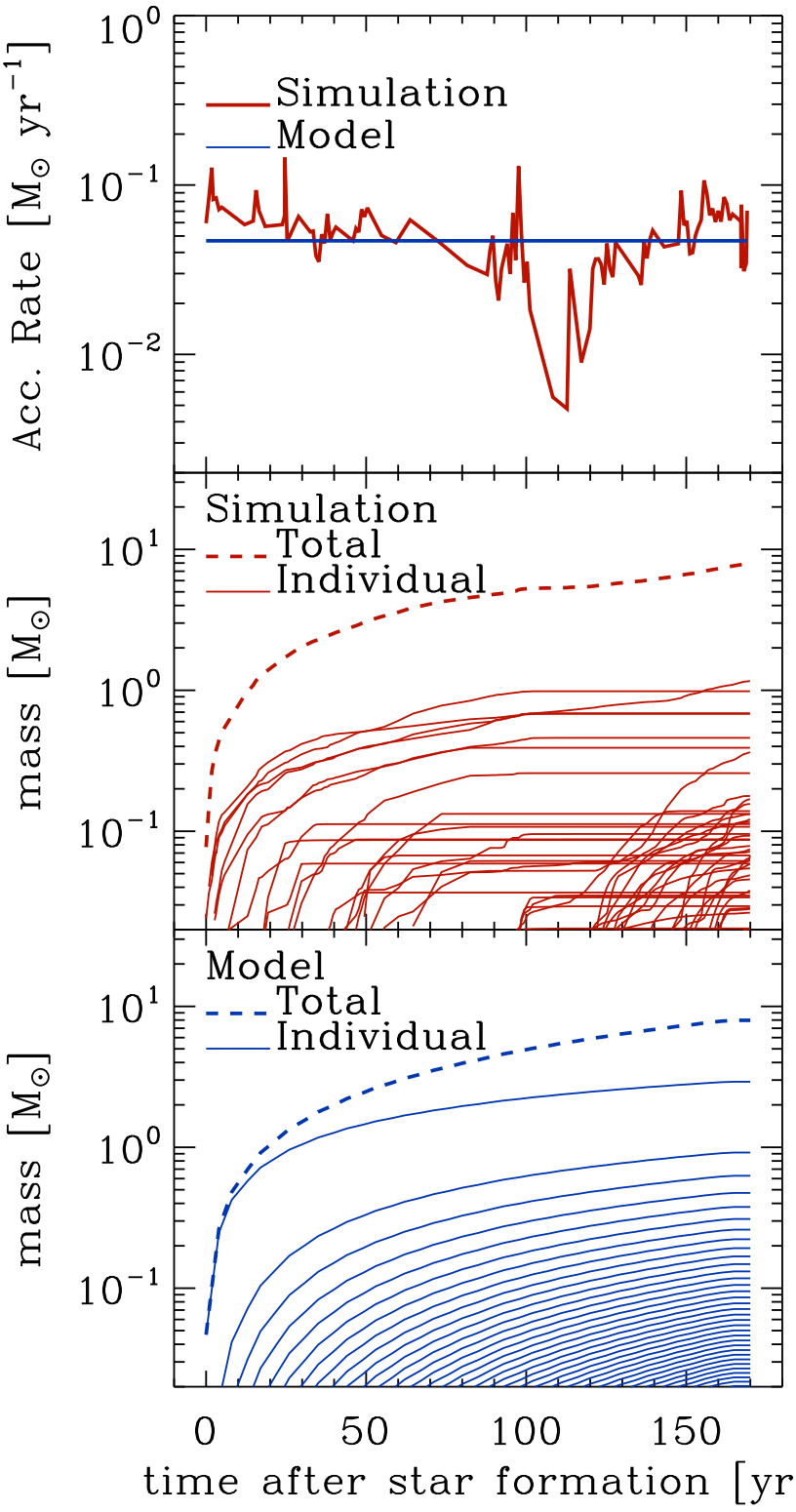

Figure 4.11: Comparison between model and simulations for the simulation with $Z = 10^{-4} Z_{\odot}$. In the top panel, we show the total mass accretion rate. In the middle panes, we plot individual and total (for the cluster) mass for the sink particles in the simulation. For the bottom panel, the same is done, but for the model.

lation are expected. Firstly, the most massive object has considerable more mass (three times) in the model. Also, the formation of sink particles is more episodic, in the sense that they do not form in a constant rate, as in the model, but rather a few sink particles are formed in a short period of time, and there are long periods without sink particle formation (e.g. from year 65 to 98).

Figure 4.11 shows considerable differences in individual accretions between model and simulations. This can also explain the differences in the mass distributions (Figures 4.6 to 4.9). Further improvements in the model, such as inclusion episodic accretion, and possible starvation of some objets, might be required to better recover results from simulations.

4.4.4 Simulations of present-day star formation

We also tested our model using the simulations of present-day star formation performed by Girichidis et al. (2012). Our procedure here was the same as in the section 4.4.1, with the exception of the parameter α, that was set to be $[\alpha^-, \langle\alpha\rangle, \alpha^+] = [0.1, 0.3, 0.5]$. These values were chosen because they fitted better the final sink particle mass distribution. We just show one plot ($\dot{n}$) of the parameters for simplicity (Figure 4.12).

With the values from the median and the extremes from the 66% HDI, the cluster was reproduced using this model. The results were compared with those from the simulations in figure 4.13. These simulations work better for testing the model, because they achieved a higher number of sink particles. Here the model fitted better the distribution from the simulations. For $\alpha = 0.5$, the object with mass of approximately one solar mass could also be recovered, but the gap between $\sim 0.3 M_\odot$ and $\sim 1.0 M_\odot$ could not be reproduced. Overall, the model could reproduce well the distribution from the simulation.

4.5 IMF in young stellar clusters

In this section, we will apply the model to observations of the Orion Nebula Cluster (ONC) by Da Rio et al. (2012). They observed the ONC over a large field of view ($\gtrsim 30' \times 30'$), using colors from deep photometry in the I band, and also two filters at $\lambda \sim 753$ and 770 nm. These observations were obtained with the Wide Field Imager (WFI) on the 2.2 m MPG/ESO telescope at La Silla. The observation provide us with the number of stars (1600), the total mass of the cluster ($10^3 M_\odot$), and the approximate age (2×10^6 yr). The parameters that remain free in the model are the initial fragment mass and

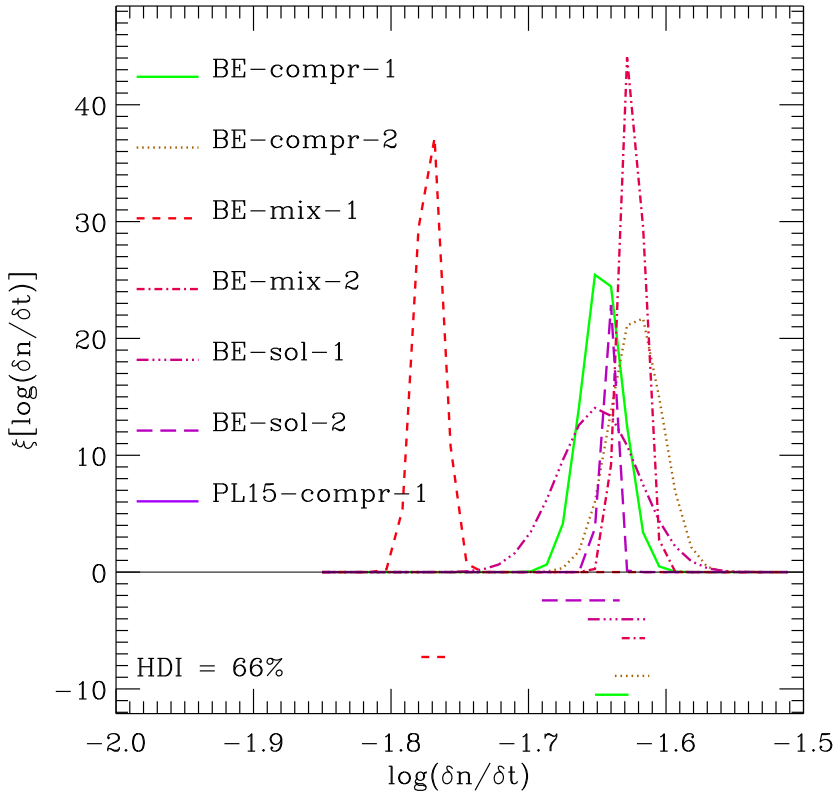

Figure 4.12: Gaussian fit for the fragmentations rate and its 66% highest probability density interval (HDI), for different mixtures of turbulent modes, random seeds, and density profile. The meaning for the acronyms of the runs are described in Girichidis et al. (2012), where the first part of the name indicates the density profile (BE for Bonnor-Ebert, and PL15 for $\rho \propto r^{-1.5}$), the letter in the middle refers to the turbulent mode ("c" for compressive, "s" for solenoidal and "m" for a natural mix of both), and the number at the end is the random seed for the turbulence.

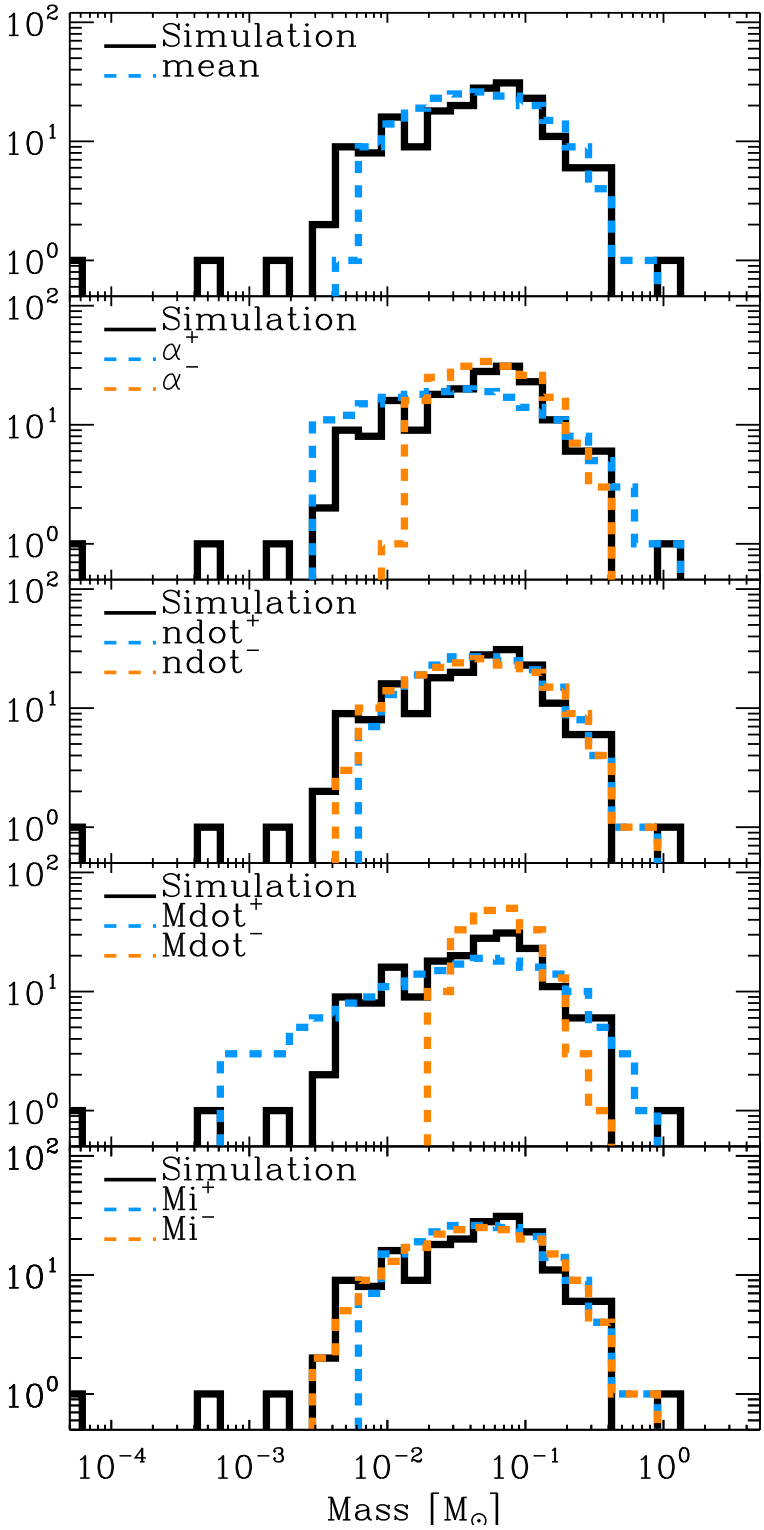

Figure 4.13: As figure 4.9, but for simulations of present-day star formation, from Girichidis et al. (2012). The particular example shown here is for their BE-mix-1, where the density distribution was that of a Bonnor-Ebert sphere, a mix of solenoidal and compressive modes was used for the turbulent forcing, and random seed number 1 was used to initiate the turbulence.

the accretion index α.

Firstly we address the influence of the initial mass in recovering the observed IMF. For that, we test whether varying the initial mass influences the predicted shape of the IMF. Many values were tested, but no strong influence was found. This can be seen in bottom panel of Figure 4.14.

Nevertheless, when we vary the accretion power α, the IMF shape changes more considerably (see middle panel in Figure 4.14). For a constant α (0.6), it was not possible to recover the peak in the distribution. Also, in this case the distribution is more spread, and values from $10^{-1.8} M_{\odot}$ to $1 M_{\odot}$ have similar numbers.

When we allow α to vary in time, however, we can find very different results. For the case that α varies from 0 (on the beginning $t = 0$) to 1(on the end $t = 2 \times 10^6$ yr), the IMF assumes an interesting shape, with a peak in very low-masses and another at masses higher than $1 M_{\odot}$. Conversely, for the case that α varies from 1(at $t = 0$) to 0(at $t = 2 \times 10^6$ yr), we get the distribution that better agree with the observation. For $\alpha = 0$, all stars accrete at the same rate, independent of their masses. On the other hand, for $\alpha = 1$, they will accrete proportional to their masses.

The model does not explain, however, why it is needed that α varies from 1 to 0 in order to recover the observations. In the competitive accretion picture, both stellar and gas dominated potentials have $\alpha > 1$. One possibility would be to assume that the objects accrete in a gas dominated potential with a density profile $\rho \propto R^{-a}$, with a $a < 4/3$ (see Bonnell et al. 2001b, equation 15).

Finally, the top panel shows the effect of varying the average stellar mass. For that, we keep the total mass constant at $M_T = 10^3 M_{\odot}$, and vary the number of stars, accordingly. This was done more as an exercise, since we know the true value from the observations. The results however could be used to predict an IMF that fits in the picture of a top/bottom-heavy IMF to explain observations (Marks et al. 2012; Kroupa et al. 2011; Suda et al. 2012, see Section 4.3).

From this analysis we conclude that the model can indeed reproduce the IMF of young stellar clusters. However the necessity to vary α could not be explained in physical therms, and more studies to address the variability of α are required.

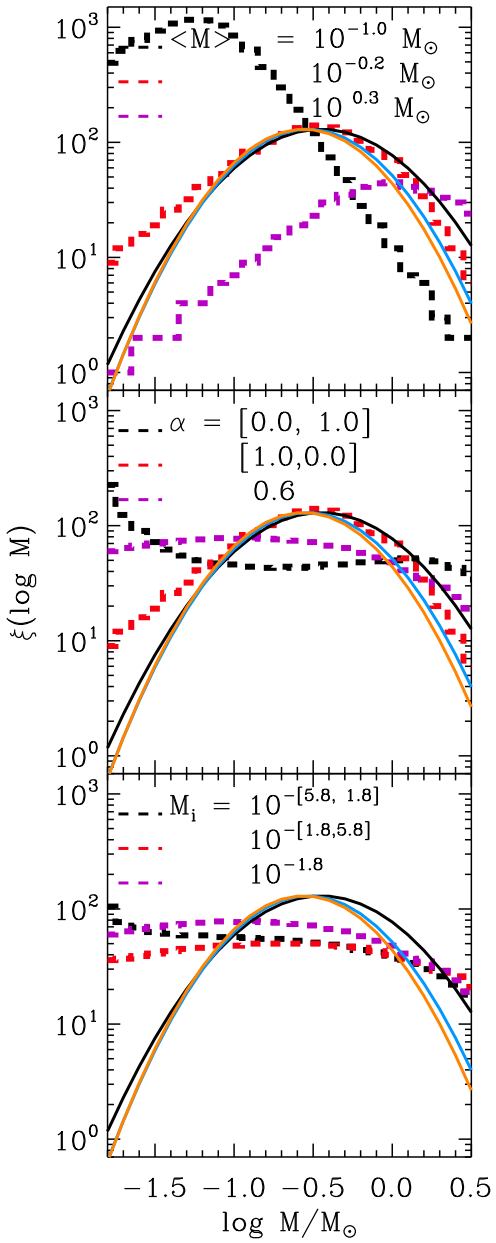

Figure 4.14: Comparison between this model and the stellar IMF calculated from observations for the ONC. The bottom panel shows the effect of varying the initial mass. The middle panes shows the influence of varying the accretion power α, and the top for the average stellar mass. The assumed age is age $= 2\times10^{-6}$ yr, the total mass is $M_T = 10^3 M_\odot$, the number of stars is the same as in the observations $N_* = 1600$ stars. For the top panel, we vary the average mass, and therefore the number of stars accordingly. For the bottom panel, α is set to 0, and the initial mass varies in $M_i = 10^{-[[4.5,1.7],[1.7,4.5],[1.7,1.7]]} M_\odot$, from $t = 0$ to $t = 10^6$ yr. The three solid lines indicate the IMF calculated assuming Baraffe et al. (1998) black and blue, where the last includes stars located above the 1 Myr isochrone. The orange solid line denotes D'Antona & Mazzitelli (1998) models.

Chapter 5

Conclusion and outlook

In this thesis we have addressed the question of what are the physical mechanisms that shape the stellar initial mass function at very low metallicities. For this purpose we performed numerical simulations to follow the thermodynamical and chemical evolution of collapsing clouds. Also, we developed a new semi-analytical model that recovers the stellar mass distributions for simulations and observations.

The simulations were done with an extended version of the Gadget 2 SPH code, with a chemical model that included a primordial chemical network together with a description of dust evolution, where the dust temperature was calculated by solving self-consistently the thermal energy equilibrium equation (Equation 2.3).

Moreover, we performed a set of eight simulations, two at low resolution and four at high resolution (Table 2.1). All simulations had an initial cloud mass of 1000 $M_{\odot}$, number density of 10^5 cm^{-3}, and temperature of 300K. We tested four different metallicities (10^{-4}, 10^{-5}, $10^{-6} Z_{\odot}$, and metal-free), and also the inclusion of small amounts of turbulent and rotational energies.

Also, we found that dust can cool the gas, for number densities higher than 10^{11}, 10^{12}, and 3×10^{13}cm^{-3} for Z $= 10^{-4}$, 10^{-5}, and 10^{-6} Z$_{\odot}$, respectively. Higher metallicity implies larger dust-to-gas fraction, and consequently stronger cooling. Therefore, the fragmentation behavior of the gas depends on the metallicity, and higher metallicities lead to a faster collapse.

For example, the characteristic fragment mass was lower for $Z = 10^{-4}$ Z$_{\odot}$, since a lower temperature reduces the Bonnor-Ebert masses at the point where the gas undergoes fragmentation. This also implies a lower ratio of fragmentation and accretion time, $t_{\rm frag}/t_{\rm acc}$, which will lead to a mass function dominated by low-mass objects. For Z $\leq 10^{-5}$ Z$_{\odot}$, fragmentation and accretion timescales are comparable, and the resulting mass spectrum is rather

flat, with roughly equal numbers of stars in each mass bin.

For the low resolution case, we tested the effect of adding turbulence and rotation. These diminish the infall velocity, leading to different fluid elements undergoing different amounts of compressional heating. This lack of heating allows the gas to reach a lower temperature. We found that the transport of angular momentum to smaller scales lead to the formation of a disk-like structure, which then fragmented into a number of low mass objects.

In addition to that, dust cooling appears to be insufficient to change the stellar mass distribution for the $Z = 10^{-5}$ and 10^{-6} $Z_\odot$ cases, when compared with the metal-free case. This can be seen in the sink particle mass function (Figure 3.7), which shows that the $Z \leq 10^{-5}$ $Z_\odot$ cases do not appear to be fundamentally different.

Therefore, we conclude that the dust is not an efficient coolant at metallicities below or equal to $Z_{crit} = 10^{-5} Z_\odot$, in the sense that it cannot change the fragmentation behavior for these metallicities. Our results support the idea that low-mass fragments can form in the absence of metals, and clouds with $Z \lesssim Z_{crit}$ will form a cluster with a flat IMF.

As for the new model for the stellar IMF, we have shown that it can recover results from simulations and observations. The model included a simple prescription to build up the IMF. We started by making use of five free parameters, but after the analysis, it became clear that two of those could be lost. On the end, the model required only three free parameters ($\langle M \rangle$, α, and time). Moreover, we did not have to make any assumption on the dominant physical mechanism which shape the IMF, making the model suitable to many environments, where the IMF could possibly change. This represents an improvement upon previous models, since they were restricted to the canonical IMF.

With such model, we were able to improve upon the analysis in our previous works, by making predictions on the future of the stellar mass distribution in simulations. Results from simulations could be simply recovered by assuming the average values for the model parameters, which were calculated from the simulations. With this model, it was also possible to compare individual and total mass accretion for the simulations.

Pursuing this further, to recover the observed IMF for the Orion Nebulae Cluster, it was necessary to vary the parameter α from 1 (in the beginning of star formation) to 0 (at the end). This means that, if one assumes that the cluster formation could be represented by the model, the accretion must have varied from a mode where the most massive stars accrete more, to a mode where all stars accrete evenly. Finally, we found that the resultant stellar mass distribution is highly dependent on the characteristic mass of the cluster, and the mode of accretion. This means that not all values for

parameters on the model would lead to a canonical (log-normal plus power-law) shaped IMF.

In conclusion, the physical mechanisms that shape the stellar IMF at very low metallicity are the ones that determine the characteristic mass and the mode of star formation. With the simulations, we were able to determine that the thermodynamical evolution of the gas during the collapse can set the characteristic mass of stars. In particular, dust cooling can change such value, thus also changing the IMF. Nevertheless, the mode of accretion, represented by the parameter α in the model, was not affected by the parameters in the simulation (see Figure 4.1), and more studies are required.

Bibliography

Abel, T., Bryan, G. L., & Norman, M. L. 2002, Science, 295, 93

Alexander, D. R., Augason, G. C., & Johnson, H. R. 1989, ApJ, 345, 1014

Banerjee, R., Pudritz, R. E., & Anderson, D. W. 2006, MNRAS, 373, 1091

Baraffe, I., Chabrier, G., Allard, F., & Hauschildt, P. H. 1998, A&A, 337, 403

Barkana, R. & Loeb, A. 2001, Phys. Rep., 349, 125

Bastian, N., Covey, K. R., & Meyer, M. R. 2010, ARA&A, 48, 339

Bate, M. R., Bonnell, I. A., & Price, N. M. 1995a, MNRAS, 277, 362

Bate, M. R., Bonnell, I. A., & Price, N. M. 1995b, MNRAS, 277, 362

Bate, M. R. & Burkert, A. 1997, MNRAS, 288, 1060

Bauer, A. & Springel, V. 2011, ArXiv e-prints

Bell, K. R. & Lin, D. N. C. 1994, ApJ, 427, 987

Bianchi, S. & Schneider, R. 2007, MNRAS, 378, 973

Binney, J. & Tremaine, S. 2008, Galactic Dynamics: Second Edition (Princeton University Press)

Bodenheimer, P. 1978, ApJ, 224, 488

Bondi, H. & Hoyle, F. 1944, MNRAS, 104, 273

Bonnell, I. A., Bate, M. R., Clarke, C. J., & Pringle, J. E. 2001a, MNRAS, 323, 785

Bonnell, I. A., Clarke, C. J., Bate, M. R., & Pringle, J. E. 2001b, MNRAS, 324, 573

Bonnell, I. A., Larson, R. B., & Zinnecker, H. 2007, Protostars and Planets V, 149

Bonnell, I. A., Smith, R. J., Clark, P. C., & Bate, M. R. 2011, MNRAS, 410, 2339

Bonnor, W. B. 1956, MNRAS, 116, 351

Bromm, V., Coppi, P. S., & Larson, R. B. 2002, ApJ, 564, 23

Bromm, V., Ferrara, A., Coppi, P. S., & Larson, R. B. 2001, MNRAS, 328, 969

Bromm, V. & Larson, R. B. 2004, ARA&A, 42, 79

Bromm, V. & Loeb, A. 2003, Nature, 425, 812

Bromm, V., Yoshida, N., Hernquist, L., & McKee, C. F. 2009, Nature, 459, 49

Caffau, E., Bonifacio, P., François, P., et al. 2011, Nature, 477, 67

Cazaux, S. & Spaans, M. 2009, A&A, 496, 365

Chabrier, G. 2003, PASP, 115, 763

Chabrier, G. & Hennebelle, P. 2011, A&A, 534, A106

Clark, P. C., Glover, S. C. O., & Klessen, R. S. 2008, ApJ, 672, 757

Clark, P. C., Glover, S. C. O., Klessen, R. S., & Bromm, V. 2011a, ApJ, 727, 110

Clark, P. C., Glover, S. C. O., Smith, R. J., et al. 2011b, Science, 331, 1040

Cramér, H. 1946, Mathematical Methods of Statistics, Vol. 9 (Princeton Mathematical Series), 575

Cullen, L. & Dehnen, W. 2010, MNRAS, 408, 669

Da Rio, N., Robberto, M., Hillenbrand, L. A., Henning, T., & Stassun, K. G. 2012, ApJ, 748, 14

D'Antona, F. & Mazzitelli, I. 1998, in Astronomical Society of the Pacific Conference Series, Vol. 134, Brown Dwarfs and Extrasolar Planets, ed. R. Rebolo, E. L. Martin, & M. R. Zapatero Osorio, 442

Dopcke, G., Glover, S. C. O., Clark, P. C., & Klessen, R. S. 2011, ApJ, 729, L3

Dopcke, G., Glover, S. C. O., Clark, P. C., & Klessen, R. S. 2012, ArXiv 1203.6842

Ebert, R. 1955, ZAp, 37, 217

Federrath, C., Chabrier, G., Schober, J., et al. 2011a, Physical Review Letters, 107, 114504

Federrath, C., Sur, S., Schleicher, D. R. G., Banerjee, R., & Klessen, R. S. 2011b, ApJ, 731, 62

Ferrini, F., Penco, U., & Palla, F. 1990, A&A, 231, 391

Frebel, A., Johnson, J. L., & Bromm, V. 2007, MNRAS, 380, L40

Girichidis, P., Federrath, C., Banerjee, R., & Klessen, R. S. 2012, MNRAS, 420, 613

Glover, S. C. O. & Abel, T. 2008, MNRAS, 388, 1627

Glover, S. C. O. & Jappsen, A.-K. 2007, ApJ, 666, 1

Goldsmith, P. F. 2001, ApJ, 557, 736

Goldsmith, P. F., Bergin, E. A., & Lis, D. C. 1997, ApJ, 491, 615

Greif, T. H., Bromm, V., Clark, P. C., et al. 2012, ArXiv e-prints

Greif, T. H., Glover, S. C. O., Bromm, V., & Klessen, R. S. 2010, ApJ, 716, 510

Greif, T. H., Johnson, J. L., Klessen, R. S., & Bromm, V. 2008, MNRAS, 387, 1021

Greif, T. H., Springel, V., White, S. D. M., et al. 2011a, ApJ, 737, 75

Greif, T. H., White, S. D. M., Klessen, R. S., & Springel, V. 2011b, ApJ, 736, 147

Heger, A., Fryer, C. L., Woosley, S. E., Langer, N., & Hartmann, D. H. 2003, ApJ, 591, 288

Heger, A. & Woosley, S. E. 2002, ApJ, 567, 532

Hennebelle, P. & Chabrier, G. 2008, ApJ, 684, 395

Hennebelle, P., Commerçon, B., Joos, M., et al. 2011, A&A, 528, A72

Hollenbach, D. & McKee, C. F. 1979, ApJS, 41, 555

Hosokawa, T., Omukai, K., Yoshida, N., & Yorke, H. W. 2011, Science, 334, 1250

Hoyle, F. 1953, ApJ, 118, 513

Hubber, D. A., Goodwin, S. P., & Whitworth, A. P. 2006, A&A, 450, 881

Jappsen, A.-K., Klessen, R. S., Glover, S. C. O., & Mac Low, M.-M. 2009a, ApJ, 696, 1065

Jappsen, A.-K., Klessen, R. S., Larson, R. B., Li, Y., & Mac Low, M.-M. 2005, A&A, 435, 611

Jappsen, A.-K., Mac Low, M.-M., Glover, S. C. O., Klessen, R. S., & Kitsionas, S. 2009b, ApJ, 694, 1161

Jeans, J. H. 1902, Royal Society of London Philosophical Transactions Series A, 199, 1

Johnson, J. L. & Khochfar, S. 2011, MNRAS, 413, 1184

Kroupa, P. 2002, Science, 295, 82

Kroupa, P., Weidner, C., Pflamm-Altenburg, J., et al. 2011, ArXiv e-prints

Krumholz, M. R. 2011, ApJ, 743, 110

Lai, D. K., Bolte, M., Johnson, J. A., et al. 2008, ApJ, 681, 1524

Larson, R. B. 2005, MNRAS, 359, 211

Latif, M. A., Schleicher, D. R. G., & Spaans, M. 2012, A&A, 540, A101

Lin, D. N. C. & Papaloizou, J. 1985, in Protostars and Planets II, ed. D. C. Black & M. S. Matthews, 981–1072

Marks, M., Kroupa, P., Dabringhausen, J., & Pawlowski, M. S. 2012, MNRAS, 422, 2246

Mayer, M. & Duschl, W. J. 2005, MNRAS, 358, 614

Miller, G. E. & Scalo, J. M. 1979, ApJS, 41, 513

Nozawa, T., Kozasa, T., & Habe, A. 2006, ApJ, 648, 435

Nozawa, T., Kozasa, T., Umeda, H., Maeda, K., & Nomoto, K. 2003, ApJ, 598, 785

Omukai, K. 2000, ApJ, 534, 809

Omukai, K., Hosokawa, T., & Yoshida, N. 2010, ApJ, 722, 1793

Omukai, K., Tsuribe, T., Schneider, R., & Ferrara, A. 2005, ApJ, 626, 627

O'Shea, B. W. & Norman, M. L. 2007, ApJ, 654, 66

Peters, T., Banerjee, R., Klessen, R. S., & Mac Low, M.-M. 2011, ApJ, 729, 72

Peters, T., Schleicher, D. R. G., Klessen, R. S., et al. 2012, ApJ, 760, L28

Pollack, J. B., Hollenbach, D., Beckwith, S., et al. 1994, ApJ, 421, 615

Press, W. H. & Schechter, P. 1974, ApJ, 187, 425

Price, D. J. & Federrath, C. 2010, MNRAS, 406, 1659

Reed, D. S., Bower, R., Frenk, C. S., et al. 2005, MNRAS, 363, 393

Rees, M. J. 1976, MNRAS, 176, 483

Salpeter, E. E. 1955, ApJ, 121, 161

Santoro, F. & Shull, J. M. 2006, ApJ, 643, 26

Schleicher, D. R. G., Banerjee, R., & Klessen, R. S. 2008, Phys. Rev. D, 78, 083005

Schleicher, D. R. G., Banerjee, R., Sur, S., et al. 2010a, A&A, 522, A115

Schleicher, D. R. G., Galli, D., Glover, S. C. O., et al. 2009, ApJ, 703, 1096

Schleicher, D. R. G., Spaans, M., & Glover, S. C. O. 2010b, ApJ, 712, L69

Schneider, R., Ferrara, A., Natarajan, P., & Omukai, K. 2002, ApJ, 571, 30

Schneider, R. & Omukai, K. 2010, MNRAS, 402, 429

Schneider, R., Omukai, K., Bianchi, S., & Valiante, R. 2012, MNRAS, 419, 1566

Schneider, R., Omukai, K., Inoue, A. K., & Ferrara, A. 2006, MNRAS, 369, 1437

Schober, J., Schleicher, D., Federrath, C., Klessen, R., & Banerjee, R. 2012, Phys. Rev. E, 85, 026303

Semenov, D., Henning, T., Helling, C., Ilgner, M., & Sedlmayr, E. 2003, A&A, 410, 611

Silk, J. 1977, ApJ, 214, 152

Smith, B. D. & Sigurdsson, S. 2007, ApJ, 661, L5

Smith, B. D., Turk, M. J., Sigurdsson, S., O'Shea, B. W., & Norman, M. L. 2009a, ApJ, 691, 441

Smith, R. J., Clark, P. C., & Bonnell, I. A. 2009b, MNRAS, 396, 830

Smith, R. J., Glover, S. C. O., Clark, P. C., Greif, T., & Klessen, R. S. 2011, MNRAS, 414, 3633

Smith, R. J., Hosokawa, T., Omukai, K., Glover, S. C. O., & Klessen, R. S. 2012, MNRAS, 424, 457

Springel, V. 2005, MNRAS, 364, 1105

Stahler, S. W., Palla, F., & Salpeter, E. E. 1986, ApJ, 302, 590

Stamatellos, D. & Whitworth, A. P. 2009, MNRAS, 392, 413

Stamatellos, D., Whitworth, A. P., Bisbas, T., & Goodwin, S. 2007, A&A, 475, 37

Suda, T., Komiya, Y., Aoki, W., et al. 2012, in Astronomical Society of the Pacific Conference Series, Vol. 458, Galactic Archaeology: Near-Field Cosmology and the Formation of the Milky Way, ed. W. Aoki, M. Ishigaki, T. Suda, T. Tsujimoto, & N. Arimoto, 65

Sur, S., Schleicher, D. R. G., Banerjee, R., Federrath, C., & Klessen, R. S. 2010, ApJ, 721, L134

Tafelmeyer, M., Jablonka, P., Hill, V., et al. 2010, A&A, 524, A58

Todini, P. & Ferrara, A. 2001, MNRAS, 325, 726

Tohline, J. E. 1980, ApJ, 239, 417

Tsuribe, T. & Omukai, K. 2006, ApJ, 642, L61

Tsuribe, T. & Omukai, K. 2008, ApJ, 676, L45

Turk, M. J., Oishi, J. S., Abel, T., & Bryan, G. L. 2012, ApJ, 745, 154

Whitworth, A. P. 1998, MNRAS, 296, 442

Wise, J. H. & Abel, T. 2007, ApJ, 665, 899

Yoshida, N., Omukai, K., & Hernquist, L. 2008, Science, 321, 669

Zinnecker, H. 1984, MNRAS, 210, 43

Acknowledgments

First and foremost I would like to express my sincere gratitude for the guidance of my supervisor Prof. Ralf Klessen. It is with immense gratitude that I acknowledge the support and help of my co-advisors Simon Glover and Paul Clark. I should also extend my gratitude to Prof. Cornelis Petrus Dullemond, who participated in my thesis committee and contributed with important advices. For their most valuable contribution in refereeing this thesis, I would like to thank Prof. Matthias Bartelmann, Prof. Eva K. Grebel, and Prof. Andrea V. Macciò.

This thesis would not have been possible without the help of several individuals who in one way or another contributed in the preparation and completion of this study. For his advises as a friend and colleague, I would like to express my gratitude to Rahul Shetty. Milica Micic, for her friendship. I am indebted to my many friends who supported me, specially Faviola Molina, Lukas Konstandin, and Paola Pinilla. I would like to extend this thanks to all my colleagues at ITA, specially Philipp Girichidis, Daniel Seifried, Robi Banerjee, Richard Allison, Christian Baczynski, Jayanta Dutta, Mei Sasaki, Jennifer Schober, Rowan Smith, Laszlo Szucs, and Ana Valente. Prof. Dominik Schleicher, for his support in the latest stages of the PhD. Secretary Anna Zacheus, for her support on understanding German bureaucracy. I would like to acknowledge the teaching from all professors at Heidelberg University.

I owe my deepest gratitude to Pilar, to whom I dedicate this thesis, for her love. This thesis would not have been possible without the unconditional support and love of my parents Edgar and Helena. My brother Jonas, for his support and friendship. My friends Denise Rocha Gonçalves, Fernando R. Reichert, Gabriela Trópia, and Tiago Boldrin, for their always present friendship. My former supervisor Gustavo F. Porto de Mello, for making astronomy always interesting and fun.